Dynamic defect morphology and hydrodynamics of sheared nematic polymers in two space dimensions

Xiaofeng Yang[a)]

Department of Mathematics, University of North Carolina at Chapel Hill, Chapel Hill, North Carolina 27599-3250

M. Gregory Forest[b)]

Department of Mathematics, Institute for Advanced Materials, Nanoscience and Technology, University of North Carolina at Chapel Hill, Chapel Hill, North Carolina 27599-3250

William Mullins[c)]

Department of Mathematics, University of North Carolina at Chapel Hill, Chapel Hill, North Carolina 27599-3250

Qi Wang[d)]

Department of Mathematics, University of South Carolina, Columbia, South Carolina 29208 and Department of Mathematics, Florida State University, Tallahassee, Florida 32306-4510

(Received 3 June 2008; final revision received 6 February 2009)

Synopsis

Dynamic (unsteady) defect structures arising in the hydrodynamics of sheared nematic polymers are investigated by numerical simulations and real-time diagnostics in two space dimensions. We simulate the Larson–Mead experiments on roll-cell formation and breakup, following recent numerical studies with a similar model [Klein *et al.*, Phys. Fluids **19**, 023101 (2007a); Klein, D. H., Ph.D. thesis, University of California, Santa Barbara (2007b)]. The simulations are blindly monitored on the basis of tensorial defect metrics defined by eigenvalue degeneracies, which are local in space and time, and monitored cost free. The focus in the defect detection is shifted from topology to local conditions, yet the nonlocality of defect domains is recovered by graphics of metric level sets. These tools reveal the spawning of an array of *oblate defect core domains*, which then deform, propagate, collide, merge, and split in a dynamic process that numerically continues *ad infinitum*. Next, we paint topological features onto snapshots of the level set texture of the oblate metric, using the remainder of the tensor information: first, the full tensor morphology (triaxial ellipsoids per grid point), and then the principal axis (where identifiable) of each

[a)]Electronic mail: xfyang@email.unc.edu
[b)]Author to whom correspondence should be addressed; electronic mail: forest@amath.unc.edu
[c)]Electronic mail: mullinsw@email.unc.edu
[d)]Electronic mail: qwang@math.sc.edu

orientation ellipsoid. These enhanced textures yield the traditional topological defect metric based on nonlocal winding number of the principal axis and the regularization of each apparent half integer and integer degree singularity. The most compelling predictions of these simulations and diagnostics are persistence of interacting oblate defect domains, while topology is highly transient, and coincidence of topological transitions with oblate domain merger and splitting. Finally, the coupling between orientation features and the transient primary and secondary flow are amplified with additional graphics. © *2009 The Society of Rheology.* [DOI: 10.1122/1.3089622]

I. INTRODUCTION

Defects in nematic liquids have a rich history involving theory and experiment. Leslie–Ericksen–Frank (LEF) director models of liquid crystals [cf. de Gennes and Prost (1993); Kleman and Friedel (1969); Kleman (1977); Meyer (1973)] provide a topological defect degree of planar textures based on the norm 1 director field. Landau–de Gennes orientation tensor models for liquid crystals and liquid-crystalline polymers [cf. de Gennes and Prost (1993); Forest *et al.* (1999, 2000b, 2001a); Feng and Leal (1997); Larson (1999); Rosso and Virga (1996); Sigillo *et al.* (1998); Sonnet *et al.* (1995); Tsuji and Rey (1997, 1998, 2000); Virga (1994)] provide topological degree by extracting the principal axis of the orientation tensor then applying the director metric. Microstructure-based kinetic theory [Doi (1981); Hess (1976); Doi and Edwards (1986); Marrucci and Greco (1991); Marrucci and Greco (1994); Larson (1990); Larson and Ottinger (1991); Sgalari *et al.* (2002); Sgalari *et al.* (2003); Grosso *et al.* (2001); Forest and Wang (2003); Forest *et al.* (2004a, 2004b); Forest *et al.* (2007b)] for the orientational probability distribution function (PDF) of rigid-rod nematic polymers provides defect topology by extracting the second-moment tensor of the orientational probability distribution and then applying the tensor protocol. In Landau–de Gennes and kinetic models, as well as molecular (particle) simulations, the orientation tensor affords the means to explore the defect core by identification of local disordered phases [cf. Andrienko and Allen (2000); Callan-Jones *et al.* (2006); Kralj *et al.* (2008); Schopohl and Sluckin (1987); Wincure and Rey (2006, 2007a, 2007b); Klein *et al.* (2007a); Klein (2007b); Yang *et al.* (2008); Choate *et al.* (2009)].

Experimental studies on nematic polymers in steady shear yield remarkable hydrodynamic orientational phenomena that remain poorly understood. We refer to the final chapter of Larson [Larson (1999)] and recent review articles [cf. Kroger (2004); Rey and Denn (2002); Tan and Berry (2003)]. Defects lie at the center of liquid crystal and nematic polymer phenomena [Kleman and Lavrentovich (2003)], from statics or near-equilibrium dynamics of the isotropic-nematic transition where free energy minimization principles apply, to strongly nonequilibrium conditions where the only tools at present are computational. Open issues include defect genesis, spatial extent, number density, the nature of defect cores, the role of defects in regions I, II, and III of the shear-viscosity curve of Onogi and Asada (1980), and the dynamics and fate of defects during and upon cessation of shear.

The particular phenomena of interest for the present paper derive from the classical Larson–Mead experiments [Larson and Mead (1993)] and the insights already gained from numerical simulations by director [Feng *et al.* (2001); Tao and Feng (2003)] and tensor [Klein *et al.* (2007a); Klein (2007b)] orientation models with full hydrodynamic coupling. Flow features include steady roll cells in the secondary flow field (transverse to the direction of plate motion) at very low plate speeds followed by a transition to unsteady flow with increased bulk shear rate. The orientational features that accompany these flow phenomena include: in the steady roll-cell regime, steady nematic distortions where the principal axis of orientation slowly varies across the flow gradient-vorticity

plane; then, as the bulk shear rate is increased, the unsteady transition is accompanied by apparent defect nucleation, propagation, splitting, reformation, and other complex phenomena. At the very least, experiments can be interpreted better with the aid of modeling and simulations, especially in light of recent advances in experimental observations of the complex flow and orientational features in shear cell experiments [Smalyukh and Lavrentovich (2006)]. In this direction, Leal and collaborators [Klein *et al.* (2007a, 2008); Klein (2007b)] led the way in the full hydrodynamic and orientation tensor modeling of the Larson–Mead experiments [Larson and Mead (1992, 1993)].

In this paper, we revisit the two-dimensional (2D) simulations of the Leal group with a similar Doi–Marrucci–Greco (DMG) flow-orientation model and our numerical algorithms [Yang *et al.* (2008)]. The model difference arises from choices of closure rules; we refer to Forest and Wang (2003) for comparisons of various closure rules in the shear-imposed monodomain phase diagram and we refer to Heidenreich *et al.* (2008a, 2008b) for comparisons of kinetic-flow one-dimensional (1D) simulations with the model employed in this paper and with a thermodynamics-based tensor-flow model.

A primary emphasis of the presented paper is the implementation of tensor-based diagnostics developed over the past several years in our group for any number of space dimensions. In 2D simulations, these diagnostics are intimately related to methods applied to molecular dynamics simulations of liquid crystals [cf. Andrienko and Allen (2000); Callan-Jones *et al.* (2006)]. The key idea [conceptually from de Gennes (1969) and analytically from Schopohl and Sluckin (1987)] is that topological defects are accompanied by defect cores, where either an isotropic (fully disordered) or an oblate uniaxial (partially disordered) phase arises. Thus, why not search for defect cores first, which are trivial to detect, and then assess topology only after a positive test?

Recall that local defects arise in any space dimension, beginning from purely homogeneous phases. In the classical Onsager phase diagram for equilibria of nematic polymers with either an Onsager or Maier-Saupe intermolecular potential, the isotropic phase is the lone stable equilibrium below a critical dimensionless concentration $N=N_c^*$; for N between N_c^* and N_c^{**}, three phases coexist: an isotropic stable, an unstable prolate, and a stable prolate nematic phase. For $N>N_c^{**}$, the highly ordered stable prolate phase coexists with unstable isotropic and oblate nematic phases [Forest *et al.* (2005a, 2005b)]. The numerical experiments presented here and in Klein *et al.* (2007a) and Klein (2007b) are for $N>N_c^{**}$, i.e., in the nematic equilibrium regime.

From a computational perspective, the notion of focusing on the defect core for detection purposes has exceptional impact: nontopological disordered phases are defined by local conditions, in space and in time, which are inexpensively monitored by level set methods, thereby supplanting the laborious task of monitoring texture snapshots for topological defects. These tensorial diagnostics have many applications for the spatially 2D flow-orientation studies of interest here: for efficient defect detection and tracking (by focusing on local conditions in defect cores as the primary object); for additional dynamical issues such as nucleation and annihilation of defects, which turn out to be easily detected and monitored; and for imaging the full orientation space morphology surrounding defect cores.

Tensor nontopological diagnostics known as scalar order parameters [de Gennes and Prost (1993)] are simply the differences in principal values of the second-moment orientation tensor. Since the tensor has constant trace, any two differences can be monitored. As local analytical conditions, isotropic (both differences vanish) and oblate (the two leading eigenvalues are equal and bounded above the remaining eigenvalue) defect metrics apply independent of spatial dimension. Indeed, our group has used these order parameter metrics to characterize sheared monodomains (homogeneous phases) [cf. For-

est *et al.* (2004a, 2004b)], extensional flow-driven monodomains [cf. Forest *et al.* (2000a, 2001b)], spatially 1D nematic filament flows [Forest and Wang (1998)], 1D sheared film, defect and shear banding between parallel plates [Forest *et al.* (2004c, 2005a, 2005b, 2006, 2007a); Heidenreich *et al.* (2008a, 2008b)], elongation-induced 2D patterns [Forest *et al.* (1999)], equilibrium 2D patterns supported by short and long range elasticity potentials [Forest *et al.* (2000b, 2001a)], and finally 2D sheared films between parallel plates [here and in Yang *et al.* (2008)].

Even though the isotropic and oblate phases are unstable at rest, at sufficiently high rod volume fractions they are nonetheless fundamental in nonequilibrium processes such as shear flow. Disordered phases provide a means to regularize incompatible local ordered phases that are forced to occupy nearby spatial sites. In 1D spatially heterogeneous morphologies [Forest *et al.* (2005a, 2005b)], we identified a prominent role of the oblate defect phase in unsteady sheared structures, serving as the regularizing phase for nearby (in time and space) oriented phases which are incompatible. In Heidenreich *et al.* (2008a, 2008b), we showed the remarkable correlation between space-time nucleation of the oblate defect, pulsating hydrodynamic jets, and the local transition between tumbling (monotone rotation of the principal axis of the orientation tensor) and wagging (finite oscillation of the principal axis). This flow-defect correlation amplified one of the early studies of hydrodynamic coupling in sheared nematic polymers by Kupferman *et al.* (2000).

Our previous studies of sheared defects were below the critical space dimension where topological defects are possible. Thus, the correlation between nontopological and topological defects was delayed in our group's flow-nematic studies until [Yang *et al.* (2008)] and the present paper. The detection of topological defects through local point-wise diagnostics is based on the tacit assumption that any such structure has a core in which the apparent discontinuity of the principal axis of orientation is regularized. The seminal paper of Schopohl and Sluckin (1987) explored the disordered phases that arise in cores of $\pm\frac{1}{2}$ defects with a Landau–de Gennes tensor model, and later extended for integer degree defects by Biscari and Virga (1997), Mottram and Hogan (1997), and Sigillo *et al.* (1998). These fundamental concepts were applied in molecular simulations by Andrienko and Allen (2000) and by Callan-Jones *et al.* (2006). We note that the orientation tensor-flow simulations of de Luca and Rey (2006), Wincure and Rey (2006, 2007a, 2007b), Klein *et al.* (2007a, 2008), and Klein (2007b) monitored eigenvalue metrics of the orientation tensor. Wincure and Rey (2007a) simulated the isotropic-nematic transition without flow and clearly identified a topological defect where the core has a highly localized oblate phase. Also, Klein *et al.* (2007a) and Klein (2007b) saw a significant weakening of orientational order in the core of topological defects of integer and half-integer degree, using a scalar order parameter that is equivalent to the sum of squares of our metrics, which only detects isotropic defects.

In this paper, we show that the oblate defect phase always forms in defect cores, in favor of the isotropic phase under conditions that simulate the roll-cell instability. Furthermore, once defects are detected (through a positive test of the oblate metric), oblate defect domains persist irrespective of director topology, and therefore appear to be the fundamental signature of shear-generated defect dynamics.

We offer further motivation for these studies based on their relevance for film and mold processing of nematic polymers and nanorod dispersions. For material property characterization, the precise nature of orientational anisotropy and heterogeneity and defect morphology in particular is paramount. These questions were central in the experimental investigations and theoretical developments that were extremely active in the 1990s. Chapter 11 of Larson's book [Larson (1999)] has a detailed description of this

activity. Han and Rey (1995) were apparently the first to simulate flow-imposed, two-dimensional sheared morphology, and defect structures using a LEF director model. de Luca and Rey (2006) recently extended these results to a Landau–de Gennes tensor model of the extrusion duct of spiders, where they insert defects and then study their evolution. Yang *et al.* (2008) recently simulated *flow-imposed* 2D transient and steady sheared responses with a McMillan tensor model of plane Couette cells, where we find no evidence of creation of topological defects, suggesting flow feedback as a key mechanism.

To simulate hydrodynamic coupling—the focus of this paper—Navier–Stokes algorithms in two or three space dimensions are required coupled with the orientational model. The first 2D physical space flow-coupled parallel shear simulations with a tensor model (derived from the microstructure kinetic theory) were presented by Sgalari *et al.* (2002), with resolution in the flow and flow gradient plane. Subsequent flow-orientation simulations in the flow gradient-vorticity plane were developed to model the Larson–Mead experiments. Feng *et al.* (2001), Tao and Feng (2003) (using a director model), Sgalari *et al.* (2003), Klein *et al.* (2007a, 2008), and Klein (2007b) (with a tensor model derived from the microstructure-based kinetic theory with a Bingham closure and variable rotary diffusivity) each successfully simulated steady roll cells, their breakup, and transition to unsteady flow, coupled with topological defect nucleation, merger, and splitting. The identification of defects in each study is based on a winding number of the director or tensor principal axis of largest principal value. We shall find quite similar transient flow-orientation phenomena, not surprising since we use similar models, with new observations of defect morphology and dynamics based on an expanded set of tensor defect metrics and detection strategy.

We note that tensor order parameter metrics have been utilized in molecular simulations of liquid crystals, for confinement in a cylinder with homeotropic anchoring [Andrienko and Allen (2000)] and for the quench from an isotropic to nematic temperature [Callan-Jones *et al.* (2006)]. Wincure and Rey (2007a, 2007b) likewise used these metrics for studying defect formation in the isotropic-nematic phase transition in two space dimensions. Our simulations and those of Leal's group impose a fixed temperature or rod volume fraction and homogeneous initial data, and defects are created by the combination of imposed shear between parallel plates and orientational confinement at solid walls.

There is no theory yet that guarantees precise relationships between topological and nontopological defects in nonequilibrium states. Work cited earlier [Schopohl and Sluckin (1987); Sigillo *et al.* (1998); Kralj *et al.* (2008); Virga (1994)] developed an exact tensor defect construction for static defects; there are no guidelines as to how such static defects will deform in the presence of flow. We proceed according to simple reasoning, as discussed in Callan-Jones *et al.* (2006). Tensor models that yield topological defects do so by a dual projection of a smooth solution in full orientation space: the full tensor is projected onto its principal axis of largest principal value and then this object is projected onto a two space dimensional plane. The observed topological defect, when viewed "up" in full orientation tensor space, is regular since our model equations are basically nonlinear reaction-diffusion equations which do not exhibit singularities. The defect morphology as determined by the projection in a nonlocal 2D region therefore must be regular in the full tensor space. There are two ways this can happen. First, the apparent defect may in fact be an artifact of the 2D projection, arising from a so-called escape into the third dimension of the principal axis [Meyer (1973)]. We show illustrations of this scenario in the simulations reported here, namely, the integer defects. Second, the tensor may regularize the discontinuity in the principal axis by passing through a degeneracy of the principal axis of orientation, i.e., through a collision of either the leading two (oblate

metric) or all three (isotropic metric) principal values. This scenario involves a defect core which is either an oblate or an isotropic phase similar to the static constructions of Schopohl and Sluckin (1987), Sigillo *et al.* (1998), and Virga (1994). In the simulations presented here, we always observe oblate cores in favor of isotropic cores. The quench simulations of Callan-Jones *et al.* (2006) found evidence of both types of defect cores. In general, since we do not *a priori* know which degeneracy is preferred, we monitor all possibilities.

If the above reasoning is sound, then the strategy for detection should be switched to a *local* (in space and time) monitoring of collisions of principal values followed *after a positive test* by the dual projection of the principal axis in a planar domain and measurement of topological nonlocal defect degree. This reasoning is emphasized in the recent work of Callan-Jones *et al.* (2006). These methods have significant implications for numerical defect detection, since nontopological defect signatures are local in space and time. The metrics can be implemented automatically and with minimal computational cost by level set tracking methods, supplanting the need to generate snapshots of planar textures and manually search for topological defects. Furthermore, as we will illustrate below, the nontopological diagnostics are robust during onset, nucleation, propagation, merger, and annihilation of defects; whereas topological degree only provides information when defects are fully formed. In the present paper, we report coupled flow-orientation studies in two space dimensions on the orientation tensor model of Doi, Hess, Marrucci, and Greco, employing a high order numerical algorithm based on the spectral-Galerkin flow solver of Shen (1994) and Yang *et al.* (2008) and parallel implementation. The defect diagnostic tools are explained further in Andrienko and Allen (2000), Callan-Jones *et al.* (2006), and Yang *et al.* (2008).

II. THE LCP-FLOW MODEL AND NUMERICAL METHOD

A. The DMG model

The Doi–Hess kinetic theory describes the dynamics of rigid-rod macromolecules in a viscous solvent in terms of an orientational PDF, whereas Marrucci and Greco [Marrucci and Greco (1991); Marrucci and Greco (1994)] extended the model to include a distortional elasticity potential. While the authors developed algorithms for the Smoluchowski equation coupled to the flow equations [Forest *et al.* (2005a, 2005b)], the system is computationally prohibitive and therefore Leal's group [Feng and Leal (1997); Chaubal and Leal (1998); Feng *et al.* (1998); Sgalari *et al.* (2002); Sgalari *et al.* (2003); Klein *et al.* (2007a, 2008); Klein (2007b)] and the authors [Forest and Wang (2003); Forest *et al.* (2004c, 2006, 2007a)] pursued effective closures of the Smoluchowski equation and stress constitutive law. Rey has developed a Landau–de Gennes theory from continuum mechanical principles. The version that we adopt here features a finite aspect ratio of nematic liquid crystal molecules modeled as spheroids and a constant rotary diffusivity [Wang (2002)]. The fundamental descriptive variable of these models is the so-called *orientation tensor* $\mathbf{Q}$,

$$\mathbf{Q} = \mathbf{M} - \frac{\mathbf{I}}{3}, \quad \mathbf{M} = \langle \mathbf{mm} \rangle, \tag{2.1}$$

where the angular brackets indicate an average with respect to the PDF, $\mathbf{m}$ is a unit vector representing the direction of a rodlike molecule, and $\mathbf{I}$ is the identity tensor.

The orientation tensor is thus the traceless part of the second-moment tensor $\mathbf{M} = \langle \mathbf{mm} \rangle$ of the orientational PDF. $\mathbf{Q}$ and $\mathbf{M}$ share spectral properties, with the same eigenvectors and eigenvalues that differ by $\frac{1}{3}$. Recall that $\mathbf{M}$ is symmetric, trace 1, and

positive semidefinite, with non-negative eigenvalues $0 \le d_3 \le d_2 \le d_1 \le 1$. The orthonormal frame of eigenvectors $\mathbf{n}_i$ with semiaxes d_i therefore geometrically determines a triaxial ellipsoid at each mesoscopic location and time. *Spheres* correspond to isotropic distributions $d_1 = d_2 = d_3 = \frac{1}{3}$ with all directions of orientation equally probable; *prolate spheroids* (with two equal minor axes) correspond to uniaxial distributions $d_1 > d_2 = d_3$, such as all stable nematic equilibria; *oblate spheroids* (with two equal major axes, $d_1 = d_2 > d_3$) correspond to a defect phase in which the most likely axis of orientation lies anywhere on the circle in the plane normal to the unique minor axis associated with the principal value d_3); full *triaxial ellipsoids* correspond to biaxial orientation where all d_i are distinct. Whenever d_1 is simple, the associated peak orientation direction $\mathbf{n}_1$ is called the major director.

N.B. The stable prolate uniaxial phase ($d_1 > d_2 = d_3$), the unstable oblate uniaxial phase ($d_1 = d_2 > d_3$), and the isotropic phase ($d_1 = d_2 = d_3$) (whose stability changes with rod volume fraction), comprise all equilibria in the Onsager equilibrium phase diagram for nematic rod dispersions. These conditions are easily monitored by local metrics, the zero level sets of $d_1 - d_2$ and $d_2 - d_3$, which are relevant here for the following reason. At sufficiently high volume fractions, the partially disordered oblate phase or the fully disordered isotropic phase—although both unstable—nevertheless arise in the cores of topological defects.

The spectral representation of $\mathbf{Q}$ is

$$\mathbf{Q} = s\left[\mathbf{n}_1(\mathbf{x},t)\mathbf{n}_1(\mathbf{x},t) - \frac{\mathbf{I}}{3}\right] + \beta\left[\mathbf{n}_2(\mathbf{x},t)\mathbf{n}_2(\mathbf{x},t) - \frac{\mathbf{I}}{3}\right], \tag{2.2}$$

where $s = d_1 - d_3$ and $\beta = d_2 - d_3$. We now translate the above special phase criteria in terms of d_i to these two order parameters. First, $s \ge \beta \ge 0$, where the equalities define special configurations. Whenever $s > 0$, $\mathbf{n}_1$ is uniquely defined and called the major director; if in addition, $\beta = 0$ then the orientation is uniaxial, whereas $\beta > 0$ corresponds to biaxial phases. Orientational degeneracies or disordered phases correspond to phases where a unique major director is not identifiable: the *oblate phase* satisfies $s = \beta > 0$ while the isotropic phase satisfies $s = \beta = 0$. Geometrically, the tensors of these disordered phase conditions correspond to oblate spheroids and spheres, respectively, which are easily identifiable in the graphics. Thus, by blind monitoring of two scalar metrics $d_1 - d_2$ and $d_2 - d_3$, an oblate or isotropic defect core is detected locally in space and time. At times with positive tests, a snapshot of the ellipsoids gives a full orientation space texture, where "platelets" identify oblate defect cores and spheres identify isotropic defect cores. Finally, a projection of the principal axis (where identifiable) onto the texture plane gives the director field topology surrounding each core.

We label "in-plane" (ϕ) and "out-of-plane" (ψ) angles of the major director $\mathbf{n}_1$ defined with respect to the flow coordinates (x is the flow direction, y is the velocity-gradient direction, and z is the vorticity axis): $\mathbf{n}_1 = (\cos\psi\cos\phi, \cos\psi\sin\phi, \sin\psi)$. Note that $\psi = 0$ corresponds to in-plane orientation where $\mathbf{n}_1$ lies in the shear plane (x,y), while $\psi = \pi/2$ corresponds to vorticity alignment of $\mathbf{n}_1$, also known as logrolling alignment. These logrolling anchoring conditions at the plates are indicated by the Larson–Mead experiments used by Klein *et al.* (2007a, 2008), Klein (2007b), and Yang *et al.* (2008) and applied in this paper.

B. Model equations

We nondimensionalize the DMG model using the gap height $2h$, the nematic rotational diffusion time scale t_n, and the characteristic stress $\tau_0=\rho h^2/t_n^2$ where ρ is the density of the nematic polymer liquid. The dimensionless velocity, position, time, stress, and pressure variables become

$$\tilde{\mathbf{V}}=\frac{t_n}{h}\mathbf{V},\ \tilde{\mathbf{x}}=\frac{1}{h}\mathbf{x},\ \tilde{t}=\frac{t}{t_n},\ \tilde{\tau}=\frac{\tau}{\tau_0},\ \tilde{p}=\frac{p}{\tau_0}. \tag{2.3}$$

The plates move at constant speed v_0, which defines a bulk flow time scale $t_0=h/v_0$; the average rotary diffusivity D_r of the rods defines another time scale $t_n=1/6D_r$, whose ratio defines the Deborah number $\mathrm{De}=t_n/t_0=v_0/6hD_r$. The following seven dimensionless parameters arise:

$$\mathrm{Re}=\frac{\tau_0 t_n}{\eta},\ \alpha=\frac{3ckT}{\tau_0},\ \mathrm{Er}=\frac{8h^2}{Nl^2},\ \mu_i=\frac{3ckT\zeta_i}{t_n\tau_0},\ i=1,2,3, \tag{2.4}$$

where Re is the solvent Reynolds number; the solvent viscosity is η; α measures the strength of entropy relative to kinetic energy; c is the number density of rod molecules; k is the Boltzmann constant; T is absolute temperature; Er is the Ericksen number which measures the short-range nematic potential strength relative to distortional elasticity strength, which involves the persistence length l and the dimensionless volume fraction N, which governs the strength of the Maier-Saupe intermolecular potential; $1/\mu_i$, $i=1$, 2, and 3 are the three nematic Reynolds numbers, themselves dependent on the three shape-dependent viscosity parameters due to the polymer-solvent interaction $3ckT\zeta_i$, $i=1$, 2, and 3. We drop the $\tilde{}$ on all variables; the dimensionless flow and stress constitutive equations take the following forms:

$$\frac{D\mathbf{V}}{Dt}=\nabla\cdot(-p\mathbf{I}+\tau), \tag{2.5}$$

the extra stress constitutive equation is given by

$$\begin{aligned}\tau=&\left(\frac{2}{\mathrm{Re}}+\mu_3\right)\mathbf{D}+a\alpha F(\mathbf{Q})+\frac{a\alpha}{3\ \mathrm{Er}}\left[\Delta\mathbf{Q}{:}\mathbf{Q}\left(\mathbf{Q}+\frac{\mathbf{I}}{3}\right)-\frac{1}{2}(\Delta\mathbf{Q}\mathbf{Q}+\mathbf{Q}\Delta\mathbf{Q})-\frac{1}{3}\Delta\mathbf{Q}\right]\\&+\frac{\alpha}{3\ \mathrm{Er}}\left[\frac{1}{2}(\mathbf{Q}\Delta\mathbf{Q}-\Delta\mathbf{Q}\mathbf{Q})-\frac{1}{4}(\nabla\mathbf{Q}{:}\nabla\mathbf{Q}-\nabla\nabla\mathbf{Q}{:}\mathbf{Q})\right]+\mu_1\left[\left(\mathbf{Q}+\frac{I}{3}\right)\mathbf{D}+\mathbf{D}\left(\mathbf{Q}+\frac{\mathbf{I}}{3}\right)\right]\\&+\mu_2\mathbf{D}{:}\mathbf{Q}\left(\mathbf{Q}+\frac{\mathbf{I}}{3}\right),\end{aligned} \tag{2.6}$$

where $D\mathbf{V}/Dt=\partial\mathbf{V}\partial t+(\mathbf{V}\cdot\nabla)\mathbf{V}$ is the material derivative, $\mathbf{D}=\frac{1}{2}[\nabla\mathbf{V}+(\nabla\mathbf{V})^T]$ is the symmetrized velocity-gradient tensor (rate-of-strain tensor), $a=(r^2-1)/(r^2+1)$ parametrizes the aspect ratio r of spheroidal molecules, and rotational Brownian motion and short-range excluded volume effects enter through the gradient of the Maier-Saupe potential,

$$F(\mathbf{Q})=\left(1-\frac{N}{3}\right)\mathbf{Q}-N\mathbf{Q}\cdot\mathbf{Q}+N\mathbf{Q}{:}\mathbf{Q}\left(\mathbf{Q}+\frac{\mathbf{I}}{3}\right). \tag{2.7}$$

The orientation tensor equation is

$$\frac{D\mathbf{Q}}{Dt} = \Omega\mathbf{Q} - \mathbf{Q}\Omega + a(\mathbf{D}\mathbf{Q} + \mathbf{Q}\mathbf{D}) + \frac{2a}{3}\mathbf{D} - 2a\mathbf{D}:\mathbf{Q}\left(\mathbf{Q} + \frac{\mathbf{I}}{3}\right) - \left\{F(\mathbf{Q}) + \frac{1}{3\ \mathrm{Er}}\left[\Delta\mathbf{Q}:\mathbf{Q}\left(\mathbf{Q} + \frac{\mathbf{I}}{3}\right) - \frac{1}{2}(\Delta\mathbf{Q}\mathbf{Q} + \mathbf{Q}\Delta\mathbf{Q}) - \frac{1}{3}\Delta\mathbf{Q}\right]\right\}, \tag{2.8}$$

where $D\mathbf{Q}/Dt = \partial\mathbf{Q}/\partial t + (\mathbf{V}\cdot\nabla)\mathbf{Q}$ and $\Omega = \frac{1}{2}[\nabla\mathbf{V} - (\nabla\mathbf{V})^T]$ is the vorticity tensor. Physical boundary conditions include no-slip velocity at the plates, which in dimensionless units becomes

$$\mathbf{V}|_{y=\pm h_y} = (\pm\mathrm{De}, 0, 0), \tag{2.9}$$

whereas periodic boundary conditions are imposed in the vorticity (z) direction. All velocity components, pressure, and tensor components are allowed and computed as functions of y, z, and t; the only restriction we make is to suppress dependence along the primary flow axis x.

To make contact and comparisons with Klein *et al.* (2007a, 2008) and Klein (2007b), we impose so-called logrolling boundary conditions on the orientation tensor $\mathbf{Q}$ at the solid plates: the nematic uniaxial equilibrium order parameter values $s=0.809$ and $\beta=0$ are imposed (determined from the presumed dimensionless rod volume fraction $N=6$), and the major director is fixed along the vorticity axis $\mathbf{n}_1=(0,0,1)$. For initial data, we first extend the plate orientation tensor equilibrium across the gap and then introduce a random perturbation of $O(10^{-6})$ amplitude in all orientation tensor components at each spatial site between the two plates.

C. Numerical method

For Eq. (2.8), noticing that the Laplacian operator is multiplied by the function $\mathbf{Q}$, we subtract $\Delta\mathbf{Q}$ on both of the left- and right-hand sides at the same time and impose the implicit form for the left and explicit form for the right in order to utilize the fast Poisson solver. We rewrite the systems (2.5)–(2.8) in the following form:

$$\frac{\partial\mathbf{V}(\mathbf{x},t)}{\partial t} - \frac{1}{\mathrm{Re}}\Delta\mathbf{V}(\mathbf{x},t) + \nabla p(\mathbf{x},t) = \mathbf{V}_n[\mathbf{V}(\mathbf{x},t),\mathbf{Q}(\mathbf{x},t)],$$

$$\nabla\cdot\mathbf{V}(\mathbf{x},t) = 0, \tag{2.10}$$

$$\frac{\partial\mathbf{Q}(\mathbf{x},t)}{\partial t} - \frac{1}{3\ \mathrm{Er}}\Delta\mathbf{Q}(\mathbf{x},t) = \mathbf{Q}_n[\mathbf{V}(\mathbf{x},t),\mathbf{Q}(\mathbf{x},t)] - \frac{1}{3\ \mathrm{Er}}\Delta\mathbf{Q}(\mathbf{x},t),$$

where $\mathbf{Q}_n$ and V_n contain all corresponding nonlinear terms. Assuming ϕ^k is the numerical approximation of ϕ at time $t=k\delta t$, $(\mathbf{V}^k, p^k, \mathbf{Q}^k)$ and $(\mathbf{V}^{k-1}, p^{k-1}, \mathbf{Q}^{k-1})$ are known, for the time discretization, the second-order pressure-correction scheme of the flow equation [cf. Guermond and Shen (2004)] and second-order semi-implicit scheme of the morphology equation can be described as follows:

- Find the intermediate velocity $\tilde{\mathbf{V}}^{k+1} = (\tilde{V}_x^{k+1}, \tilde{V}_y^{k+1}, \tilde{V}_z^{k+1})$ such that

$$\frac{3\tilde{\mathbf{V}}^{k+1} - 4\mathbf{V}^k + \mathbf{V}^{k-1}}{2\delta t} - \frac{1}{\mathrm{Re}}\Delta\tilde{\mathbf{V}}^{k+1} + \nabla p^k = 2\mathbf{V}_n(\mathbf{V}^k,\mathbf{Q}^k) - V_n(\mathbf{V}^{k-1},\mathbf{Q}^{k-1}),$$

$$\tilde{V}_x^{k+1}|_{y=\pm h_y} = \mathrm{De}, \tilde{V}_y^{k+1}|_{y=\pm h_y} = 0, \tilde{v}_z^{k+1}|_{y=\pm h_y} = 0. \tag{2.11}$$

- Find the auxiliary function ψ^{k+1} to satisfy

$$-\Delta\psi^{k+1} = \frac{3}{2\delta t}\nabla\cdot\tilde{\mathbf{V}}^{k+1}$$
$$\left.\frac{\partial\psi^{k+1}}{\partial y}\right|_{y=\pm h_y} = 0. \tag{2.12}$$

- Update $(p^{k+1}, \mathbf{V}^{k+1})$ by

$$p^{k+1} = p^k + \psi^{k+1} - \frac{1}{\mathrm{Re}}\nabla\cdot\tilde{\mathbf{V}}^{k+1},$$
$$\mathbf{V}^{k+1} = \tilde{\mathbf{V}}^{k+1} - \frac{2\delta t}{3}\nabla\psi^{k+1}. \tag{2.13}$$

- Find $\mathbf{Q}^{k+1}$ such that

$$\frac{3\mathbf{Q}^{k+1} - 4\mathbf{Q}^k + \mathbf{Q}^{k-1}}{2\delta t} - \frac{1}{3\ \mathrm{Er}}\Delta\mathbf{Q}^{k+1} = 2\mathbf{Q}_n(\mathbf{V}^k,\mathbf{Q}^k) - \mathbf{Q}_n(\mathbf{V}^{k-1},\mathbf{Q}^{k-1}) - \frac{1}{3\ \mathrm{Er}}\Delta\mathbf{Q}^k,$$
$$\mathbf{Q}^{k+1}|_{y=\pm h_y} = Q^0|_{y=\pm h_y}. \tag{2.14}$$

The semidiscrete scheme above provides an advantage: for each time step, we only need to solve a sequence of Poisson equations of the form,

$$u - \lambda\Delta u = f(u),$$
$$u(y,z)|_{y=\pm 1} = 0 \quad \text{or} \quad \left.\frac{\partial u(y,z)}{\partial y}\right|_{y=\pm 1} = 0. \tag{2.15}$$

To solve the above equation, we assume that the function $u(y,z)$ can be expanded in the following form, consistent with physical boundary conditions between the plates and periodicity in the vorticity direction:

$$u(y,z) = \sum_{m=-M/2}^{m=M/2} u_m(y)e^{imz}. \tag{2.16}$$

Then Eq. (2.15) yields,

$$(1+\lambda m^2)u_m(y) - \lambda u_{myy}(y) = f_m(y),$$
$$u_m(y = \pm 1) = 0 \quad \text{or} \quad \left.\frac{\partial u_m(y)}{\partial y}\right|(y = \pm 1) = 0. \tag{2.17}$$

For any fixed m, we solve the above 1D Poisson equation, as in [Shen (1994); Yang *et al.* (2008)]. In the simulations presented in this paper, the computational domain is $(y,z) \in [-h_y,h_y]\times[0,h_z]$ where h_y=1 and h_z=2, with periodicity in the z direction and physical boundary conditions at the planar plates $y = \pm h_y$. Our goal is to reproduce steady roll cells at low plate speeds followed by unsteady transitions at higher plate speeds, as seen by Larson–Mead experimentally and by Klein *et al.* (2007a) with simulations of a similar model. We identify parameter sets based on these criteria aided by comprehensive nu-

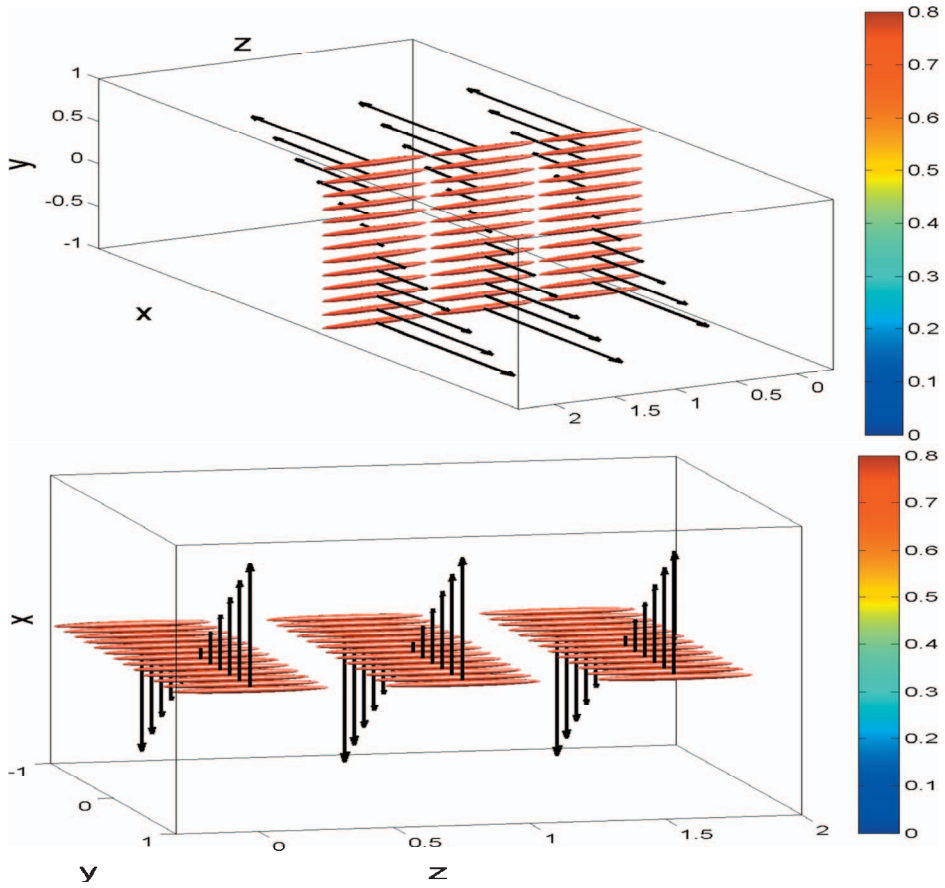

FIG. 1. Sketch of the initial condition of M ellipsoids and velocity profile (arrows). The right color bar is based on the level set values of the oblate defect metric d_1-d_2, which is consistent (~0.8) for the uniform initial conditions on orientation chosen here. The same color scale is applied throughout the paper.

merical studies of monodomain phase diagrams for variable Deborah number and 1D heterogeneous phase diagrams for variable Deborah and Ericksen numbers. The following parameter values suffice for these purposes: $a=0.8$, $\mu_1=9\times10^{-3}$, $\mu_2=9\times10^{-3}$, $\mu_3=1.0$, Re=10.0, $\alpha=2$, and Er=50. We fix the equilibrium nematic concentration $N=6$, so the equilibrium order parameter is $s_0=0.809$. This value is the baseline for how well ordered the rod ensemble is throughout the gap in our graphics. The initial flow profile and geometry of the **Q** tensor is described in Fig. 1.

We now explore the structure formation for the initial-boundary value data prescribed above, with all other parameters fixed, for variable De. In all simulations, we use 256 Fourier modes in z and 256 Legendre polynomials in z, with a time step of $\delta t=0.001$. The results presented are robust to finer resolution in space and time, as discussed in Heidenreich (2008a).

III. NUMERICAL RESULTS

We focus on the details of two particular space-time attractors: the steady roll-cell flow pattern and associated orientational morphology and then the unsteady attractor that arises at higher Deborah number from the roll-cell instability. In each simulation, we

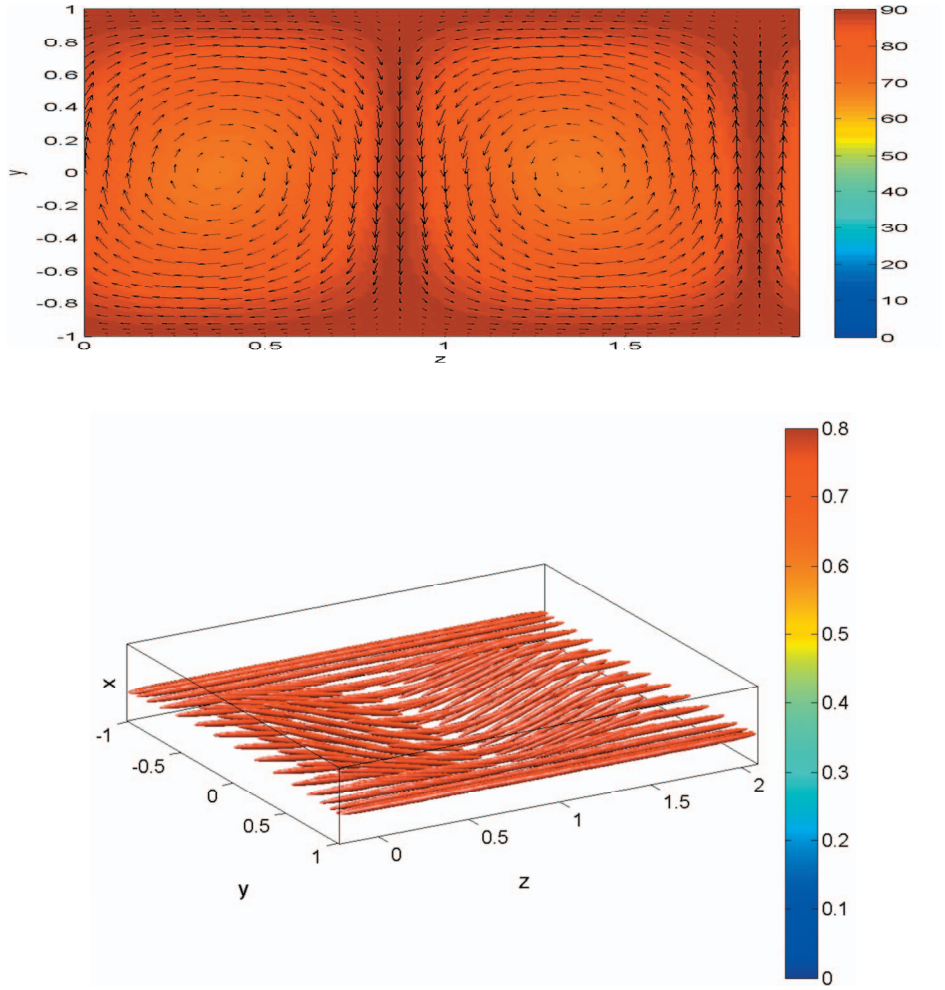

FIG. 2. 2D steady roll-cell morphology: secondary flow and orientational correlation. Top: The absolute value of the out-of-plane primary director angle ψ superimposed with the secondary flow (V_y, V_z). Bottom: The **M** ellipsoids color-coded by level set values of the oblate defect metric of $d_1 - d_2$, indicating a negative test for defects.

present correlations among the flow and principal orientation axis features, textures defined by the local defect metrics, and textures defined by the full geometry of the orientation tensor at each spatial site.

A. Stable roll cells

We begin at a low Deborah number De=1.5, where steady-state attractors are observed. The simulations converge to steady state by $t=400$, or equivalently, $\gamma=300$ strain units.

Figure 2(a) shows the absolute value of the out-of-plane angle ψ of the principal axis (major director) superimposed with the secondary flow profile (V_y, V_z), in the (y,z) texture plane, transverse to the flow direction. The terminology "roll cell" is self-evident. There are two roll cells in the physical domain, and the level sets of ψ coincide with the closed streamlines. Figure 2(b) gives the steady-state distribution of orientation tensor

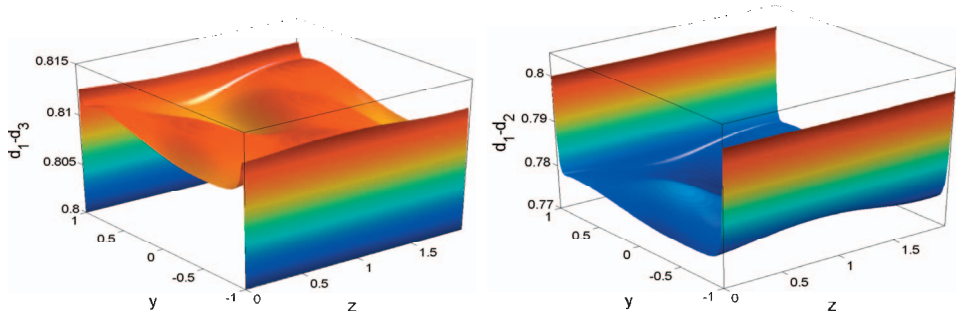

FIG. 3. 2D steady roll-cell morphology: order parameter defect diagnostics. Left: The steady isotropic defect metric d_1-d_3. Right: The steady oblate defect metric d_1-d_2. Note that each defect metric is color-coded with blue for the minimum value and red for the maximum value. Both metrics are bounded far from the zero value indicative of defects.

ellipsoids which provide full configuration space information across the 2D physical domain. The ellipsoids are color coded in terms of the primary defect metric d_1-d_2, which reinforces the information carried by the ellipsoid geometry. These graphics indicate that the orientational morphology has very weak order parameter distortions, and the structure is dominated by the rotation of the principal axis of orientation. Figure 3 gives quantitative confirmation of this morphology characterization with the steady-state values of both the isotropic metric d_1-d_3 (left) and the oblate metric d_1-d_2 (right), across the texture plane, showing variation from the equilibrium plate conditions by less than 5%. This is truly a *director-dominated steady morphology*. It is not surprising that this "director-dominated" morphology would be captured by liquid crystal LEF simulations [Feng *et al.* (2001)].

We now show the full flow features associated with the roll-cell regime, which will set the stage for transitions to more complex features at higher De. Figure 4 shows the steady-state primary velocity, the departure from pure shear (the nonlinear flow feedback), individual secondary flow components (additional flow feedback), and the pressure. If there were no flow feedback, for these boundary conditions we would have $V_x = V_x^0 = \mathrm{De} * y$, where $V_x^0 = V_x(t=0)$ is the initial condition. Since $|V_x - V_x^0|/|V_x| \sim 10^{-3}$, as seen from the scale in part (b), the primary flow is indistinguishable from pure shear. Note that the secondary flow components V_y and V_z have maximum norms on the order of 10^{-3}, while the pressure is on the order of 10^{-2}. These results again support the excellent approximation of the roll-cell formation in the LEF model simulations of Feng *et al.* (2001).

For spatial domains of aspect ratio $h_z/(2h_y)=1$, two roll-cells form at De=1.5 and Er=50. As we increase the physical domain aspect ratio, the same qualitative steady attractor persists, with an increase in the number of roll cells as follows: six cells for aspect ratio 2, ten cells for aspect ratio 4, and 20 cells for aspect ratio 8. For this paper, we are interested in the detailed features of the orientational morphology as they correlate with roll cells and then the flow-morphology correlations as roll cells destabilize and defects are spawned. We restrict this study to the spatial domain aspect ratio of 1, which reduces the number of cells. The features we report are robust to higher aspect ratios, except that the number density of prominent features is increased.

B. Unsteady transition: Roll-cell breakup and defect nucleation

We increase the Deborah number to De=3.5, retaining all other parameters fixed. The steady roll cells and orientational morphology at De=1.5 become unstable with longtime

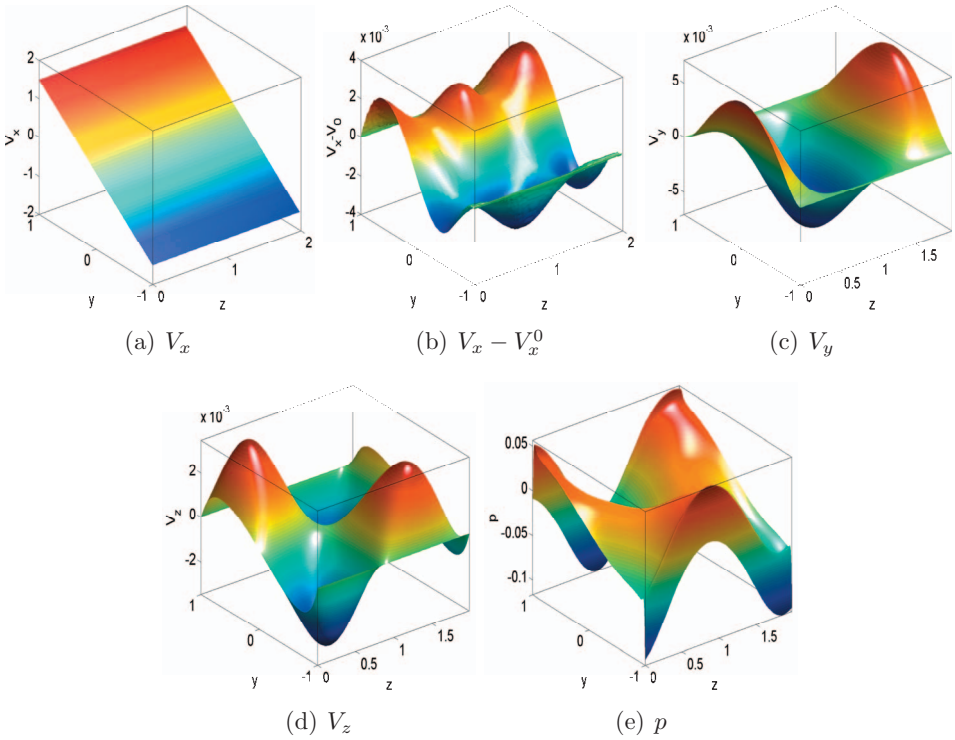

FIG. 4. 2D steady roll-cell morphology: full 2D velocity $\mathbf{V}=(V_x,V_y,V_z)$ and pressure profiles, where $V_x^0 = V_x(t=0)$, (a) V_x, (b) $V_x - V_x^0$, (c) V_y, (d) V_z, and (e) p. The color code for each quantity is blue for the minimum value and red for the maximum value.

persistence of unsteady flow and orientational morphology. The main emphasis of the present paper is to study the transient 2D attractor that results from the roll-cell instability on the basis of full tensor defect diagnostics and graphics.

Figure 5 shows the absolute value of the out-of-plane angle ψ superimposed on the secondary flow profile (V_y,V_z) at three early selected times in the simulation $t=16$, 17, 50, or equivalently in strain units $\gamma=28$, 29.75, and 87.5. Four roll-cells form at $t=16$, uncentered and asymmetric—reminiscent of Fig. 2(a)—except that the major director at the center of the cells has rotated significantly toward the shear (x,y) plane while the troughs between the cells remain almost vorticity aligned. The first panel of Fig. 5(b) gives a blowup of the domain near the top plate where two cells meet; vorticity alignment persists deep into the center of the updraft. Note further that the z gradient of ψ is again concentrated at the "updrafts" and "downdrafts" between the roll cells. The flow generation at $t=16$ is shown in the top row of Fig. 6. We find that all orientation-induced flow features are amplified by 1 order of magnitude or greater from the De=1.5 results, with maximum norms rising to the order of a few percent of the normalized plate speed De. Summarizing, we find that an increase in De from 1.5 to 3.5 has led to 1 order of magnitude increase in flow generation and stronger director gradient morphology based on the $t=16$ snapshot of the simulation. The prominent features are striped domains between the roll cells, where there is the strongest upflow or downflow toward the plates and where the director has rotated farthest from the plate orientation. The strongest orientational gradients are at the tips of the striped domains.

The next snapshot $t=17$ indicates that the secondary flow persists with four slightly

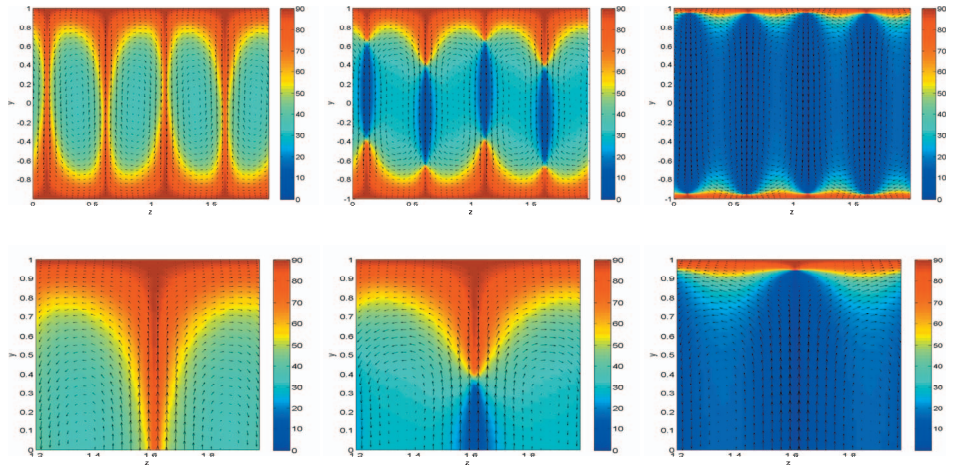

FIG. 5. Unsteady regime of roll-cell breakup: Top row: Snapshots of the absolute value of the out-of-plane angle ψ superimposed on the secondary flow profiles (V_y, V_z) at $t=16$, 17, and 50. Bottom row: Local blow up of the regions in each snapshot where a strong gradient occurs. In all six figures, the color-coding is based on the values of ψ, where dark red = 90 degrees for vorticity (z-axis) alignment and dark blue = 0 degrees for alignment somewhere in the shear (x,y) plane.

modified roll cells, but the morphology of the director angle ψ has changed dramatically, now migrating further toward the shear plane in the interior. The prominent features are cigar-shaped (dark blue) domains in the up and down drafts between roll cells, inside of which the director orientation is tilted all the way to the shear (x-y) plane. At the tips of each cigar domain, an extremely strong orientational gradient is implied: the major director varies from vorticity alignment to in-plane alignment over a very short lengthscale. From $t=16$ to $t=17$, the thin vertical strips of vorticity alignment have split, leaving

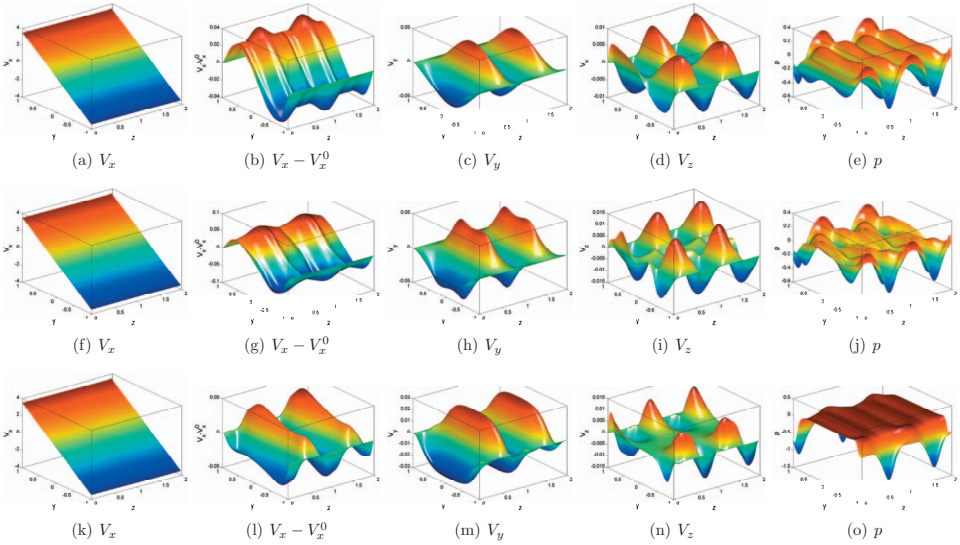

FIG. 6. Unsteady regime of roll-cell breakup: primary and secondary flow and pressure profiles at $t=16$ (top row), $t=17$ (middle row), and $t=50$ (bottom row). The color-coding in each figure interpolates between dark red for the maximum value and dark blue for the minimum of each respective function.

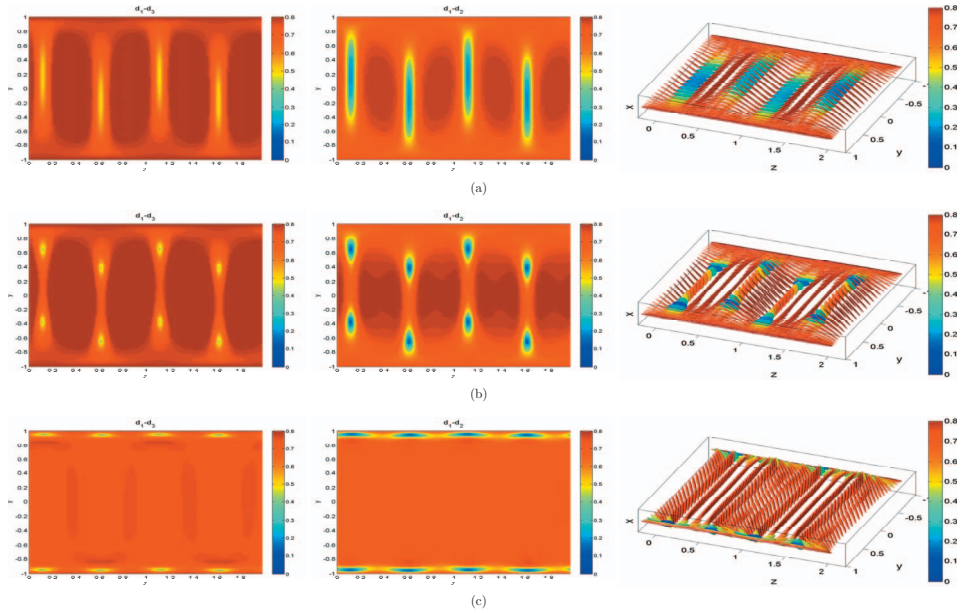

FIG. 7. Unsteady regime of roll-cell breakup. Order parameter diagnostics for isotropic defects d_1-d_3 (column 1) and oblate defects, d_1-d_2 (column 2), and **M** tensor ellipsoids color coded by level set values of the oblate defect metric d_1-d_2 (column 3), at $t=16$ (row 1), $t=17$ (row 2), and $t=50$ (row 3). N.B. Dark blue signals oblate defect domains of the level set $d_1-d_2=0$, which we conclude from the isotropic defect metric that remains well above zero.

vorticity-aligned fingers from the plate to the cigar tips, while the cigar domains have in-plane orientation. The flow features at $t=17$ are given in row 2 of Fig. 6, showing only minor qualitative differences from $t=16$. The dynamics from $t=16$ to $t=17$ are dominated by an orientational response to the quasistationary flow, with little flow changes. We return shortly to amplify the orientational morphology with enhanced diagnostics and graphics.

The $t=17$ orientation-flow structure persists for some time but eventually breaks up and settles into a dramatically different morphology shown at $t=50$. The entire texture, aside from localized plate boundary layers, has nearly in-plane orientation (i.e., the principal axis has very small vorticity axis component). The fingers at $t=17$ where $\psi=\pi/2$ have stretched and thickened, now reaching to within 0.05 normalized height units of the plates, still residing in the up and down drafts between the four quasistationary roll cells. The red regions of vorticity alignment are now localized in boundary layers near each plate, with a wavelength of variation of one fourth of the z period. The layer is blown up in panel 3 of Fig. 5(b) for comparison with the other two snapshots. The corresponding flow features at $t=50$ are shown in row 3 of Fig. 6.

1. Oblate defect cores and defect detection metrics

Figure 7 amplifies the morphology at $t=16$, 17, and 50 with graphics of the defect metrics d_1-d_2 and d_1-d_3 and of the full orientational ellipsoid representation of texture.

The isotropic defect metric d_1-d_3 is bounded away from zero at all times: *isotropic defect phases do not form*. (Level set tracking of d_1-d_3 for all times confirms these observations.) Yet, column 2 shows *oblate defect phases* which are evident in each snapshot, in geometric domains that vary in shape, size, and location precisely correlated

with strong gradients in the major director angle ψ. The oblate domains are transient: vertical stripes at $t=16$, then tear-shaped drops at $t=17$, and then thin strips along the plates at $t=50$. In the subsequent dynamics, for as long as we run the codes, oblate defect domains persist. (We turn to topology below, which will not be robust.)

The thin vertical stripes at $t=16$ and thin horizontal stripes at $t=50$ occur when the principal axis of the orientation has strong gradients that are primarily 1D: in the z direction in the narrow trough between roll cells at $t=16$, in the y direction localized near the plates at $t=50$. When the strong gradients are more localized and 2D at $t=17$, oblate defect drops form. The upshot is that *strong gradients engage the full orientation tensor*; monitoring either the order parameters or the principal axes, strong gradients are correlated. This feature is consistent with asymptotic and numerical studies of wall boundary layers in shear cells [cf. Forest *et al.* (2004c, 2006, 2007a)].

Column 3 of Fig. 7 gives the full orientational configuration space morphology through the second-moment tensor ellipsoid textures of each snapshot $t=16$, 17, and 50, clearly revealing oblate spheroids precisely in the oblate defect domains (vertical stripes, drops, and thin horizontal stripes) detected in column 2 by the zero level set metric $d_1-d_2=0$.

2. Topological metrics associated with defect cores

At this stage, we have a positive test for defect cores, and furthermore, clear evidence of dynamic transitions in the geometry, number, and location of defect domains. Next, we pursue the nonlocal topology that we suspect surrounds the defect domain cores. We again acknowledge the independent numerical work of Andrienko and Allen (2000) and Callan-Jones *et al.* (2006) and the insights gained by the analysis of Schopohl and Sluckin (1987), Sigillo *et al.* (1998), and Kralj *et al.* (2008).

We focus on the $t=50$ snapshot in Fig. 8. This structure is chosen for a detailed inspection because it persists as a quasistationary state for tens of time units. These defect structures are of two types: those nearest to the plates and those further inside the gap. We magnify each of the ellipsoidal structures by a factor of 4 from Fig. 7 in Fig. 8 column 1, panels (a) and (d). We enhance the ellipsoids with the level set color scheme of the oblate defect metric d_1-d_2 so the defect core is prominent. The double projection (of the principal axis of $\mathbf{M}$, onto the texture plane) is given below the ellipsoidal texture, with vertical solid stakes identifying the locations of topological defects. These projections possess insufficient resolution, so we next magnify the $y-z$ director projections by another factor of 4 in column 2 of Fig. 8, panels (b) and (e); the oblate defect metric d_1-d_2 is again superimposed on the director topology using an absolute color scale. We find

- *Each oblate defect core has two topological defects attached to it*: a half-integer defect residing at the center of the oblate defect (the zero level set of d_1-d_2) and an integer defect that is shifted off the oblate core center and removed from the zero level set of the oblate metric. We refer to these as *defect domain structures*, each consisting of an oblate core and an attached pair of degree $\left(+1,-\frac{1}{2}\right)$ or $\left(-1,+\frac{1}{2}\right)$ topological defects.
- The integer defects are associated with nondegenerate structures when viewed in full orientation space: the principal axis of the second-moment ellipsoid smoothly escapes into the third dimension (the primary flow direction).
- The integer defect core corresponds to a return to nearly uniaxial symmetry, with $d_2-d_3\sim 0.01$), whereas the uniaxial order parameter $s=d_1-d_3\sim 0.76$: a slightly lower value than the equilibrium value ($s=0.809$) imposed at the plates.
- The half-integer defects are associated with the algebraic degree 2 multiplicity of the maximum principal value of the orientation tensor, i.e., the oblate phase. The predomi-

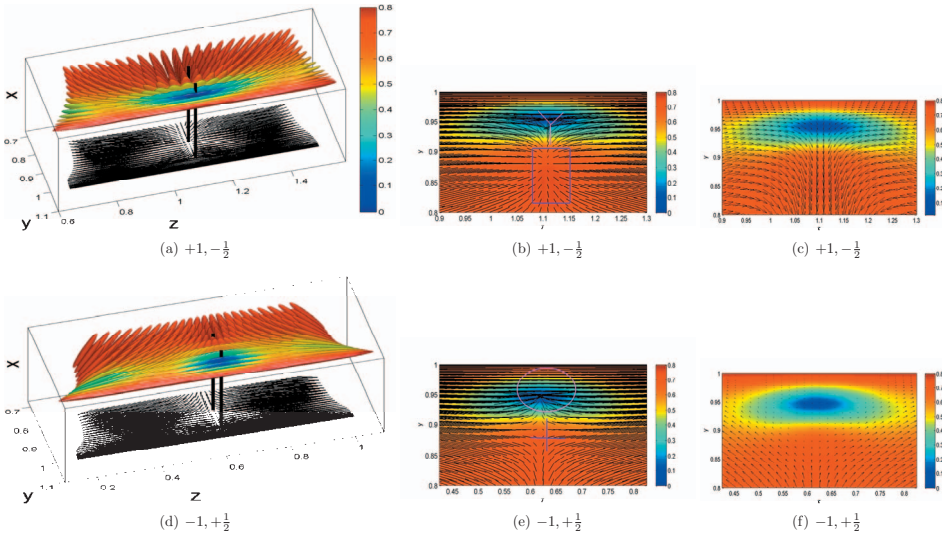

(a) $+1,-\frac{1}{2}$ (b) $+1,-\frac{1}{2}$ (c) $+1,-\frac{1}{2}$

(d) $-1,+\frac{1}{2}$ (e) $-1,+\frac{1}{2}$ (f) $-1,+\frac{1}{2}$

FIG. 8. Unsteady regime of roll-cell breakup: post-diction topological evaluation of defects from the $t=50$ snapshot in Fig. 7. The two distinct defect domain structures near the top plate are amplified: $y\sim0.95$, $z\sim1.1$, in panels (a)–(c) and $y\sim0.95$, $z\sim0.63$ in panels (d)–(f). Column 1: fourfold magnification of the ellipsoid texture together with the projection of the major ellipsoid axis onto the texture plane. Column 2: 16-fold magnification of the major director topology, superimposed with color coding by the level sets of the oblate defect metric d_1-d_2. Column 3: 16-fold magnification of the secondary flow profile, superimposed with color coding by the level sets of the oblate defect metric d_1-d_2. Topological defects are identified and labeled according to degree: +1 (square) and $-\frac{1}{2}$ (tripod) defects share one oblate defect core; -1 (cross) and $+\frac{1}{2}$ (circle) defects share the other oblate defect core. (a) $+1,-\frac{1}{2}$, (b) $+1,-\frac{1}{2}$, (c) $+1,-\frac{1}{2}$, (d) $-1,+\frac{1}{2}$, (e) $-1,+\frac{1}{2}$, and (f) $-1,+\frac{1}{2}$.

nantly planar principal axis surrounding the core defocuses to a circle of orientations at the core (the oblate phase), thereby resolving the pending singularity of the principal axis at the center of the core.

3. Secondary flow-defect morphology correlations

Column 3 of Fig. 8, panels (c) and (f), superimposes the secondary flow with the color scale of the oblate defect metric on the same scale as the director projections of panels (b) and (e). The graphics reveal

- The defect domain structures at the top plate with $\left(+1,-\frac{1}{2}\right)$ topology form at the tips of downdrafts between roll cells, nearby a stagnation point of secondary straining flow.
- The structures at the top plate with $\left(-1,+\frac{1}{2}\right)$ topology form at the tips of updrafts between roll cells, also nearby a stagnation point of secondary straining flow.

C. Oblate defect merger: Persistence of oblate domains and transition to trivial topology

The defect domain structures at $t=50$ persist for tens of time units. From $t=15$ to $t=70$, the dynamics is dominated evolution of the orientational morphology, while the hydrodynamic response is almost stationary, with a quasisteady secondary roll-cell structure and primary shear flow. Around $t=70$, there is a breakdown of the four roll-cell secondary flow pattern accompanied by a subsequent merger of neighboring pairs of

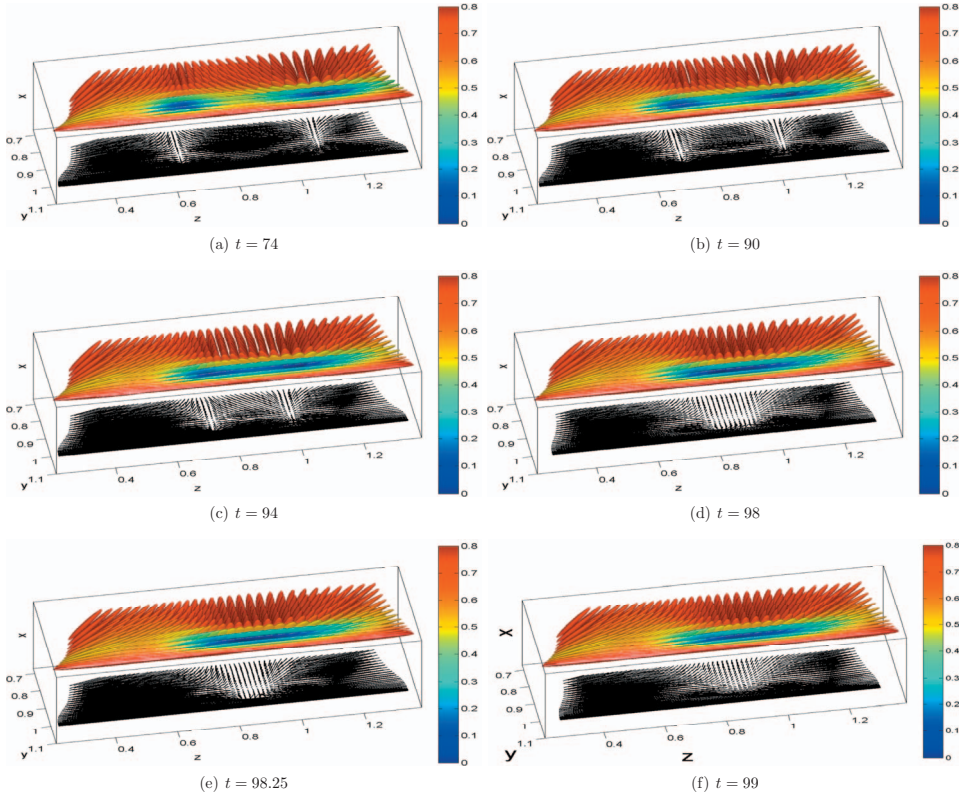

FIG. 9. Diagnostics of defect merger, annihilation of topology, and persistence of oblate domains: Two defects at t=74, their merger (t=90 to 98.25), and topological annihilation (t=99), seen through full orientational ellipsoid textures. (a) t=74, (b) t=90, (c) t=94, (d) t=98, (e) t=98.25, and (f) t=99.

defect domain structures. We emphasize that these features are tracked and depicted by low-cost level set graphics of the oblate defect metric; the isotropic metric clearly shows the smallest eigenvalue of **M** is simple throughout the simulation and will not be shown. The topology, as we shall see, is transient; whereas the oblate domains remain identifiable.

Snapshots at t=74, 90, 94, 98, 98.25, and 99 of salient flow-orientation features are presented next. Figure 9 gives the full orientation ellipsoid textures, Fig. 10 gives the superposition of the major director and the color-coded oblate defect metric d_1-d_2, and Fig. 11 superimposes the secondary flow and the out-of-plane director angle ψ. As the two oblate domains merge, the integer defects disappear because the ellipsoids whose principal axes escape into the third dimension grow from a localized "spot" to a 2D domain. Since there is no local escape of the primary director, the integer degree topology is gone. The half-integer defects disappear by t=99, as seen in the snapshots of Fig. 10, but the secondary flow is key to understanding this process. From Fig. 11, the t =74 snapshot shows that the $+\frac{1}{2}$ defect and core at (z=0.64, y=0.95) is getting swept by the secondary flow toward the $-\frac{1}{2}$ defect and core at (z=1.1, y=0.95), which is still near a stagnation point of the secondary flow. By t=90, the $+\frac{1}{2}$ defect and core are continuing to be swept to the right (increasing z), and the $-\frac{1}{2}$ defect and core are drifting left (decreasing z) along with the stagnation point in the flow. Figure 11 shows that the light green-blue domain between the two half-integer defects is shrinking in height until it is

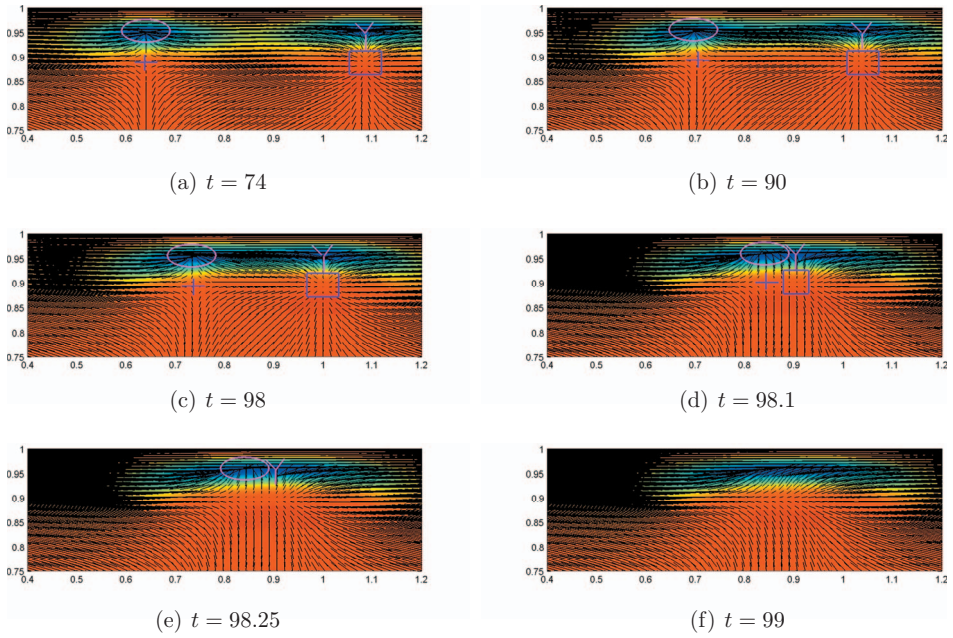

FIG. 10. Diagnostics of defect merger, annihilation of topology, and persistence of oblate domains: seen through projection of the director field superimposed with color-coded level sets of the oblate metric d_1-d_2. Topological defects: +1 (square); $-\frac{1}{2}$ (tripod); -1 (cross), and $+\frac{1}{2}$ (circle). (a) $t=74$, (b) $t=90$, (c) $t=98$, (d) $t=98.1$, (e) $t=98.25$, and (f) $t=99$.

gone at $t=98.1$. This means that the y gradients of the out-of-plane angle ψ are trapped between the merging oblate defect domains, and the opposite-signed half-integer director rotations at the center of the merging cores smoothly cancel each other until the two half-integer defects have annihilated and the topology is trivial.

The defect merger just shown corresponds to a topological transition, whereas the level sets of the oblate defect metric d_1-d_2 reveal persistence and propagation of oblate domains. *The center of the oblate domains may weaken* (the minimum of d_1-d_2 rises slightly above zero) when the topology is trivial, but the gradients of d_1-d_2 clearly remain identifiable. For the next 30 time units, the localized oblate domains remain identifiable while the surrounding topology is trivial. This phenomenon detected by level sets of the oblate metric has not been reported previously in defect morphology studies. We emphasize that the remnants of topology are tracked in this way, and we show next, these tracked oblate domains also play a leading role in the next topological transition.

D. Oblate defect domain splitting and reformation of nontrivial topology

Next, Fig. 12 (the ellipsoids), Fig. 13 (the director projection and color-coded oblate metric), and Fig. 14 (the color-coded out-of-plane angle ψ and secondary flow field) document the reformation of defect topology. The ellipsoidal texture and the oblate defect metric d_1-d_2 identify oblate domains that persist with trivial topology until $t=120$; the out-of-plane director angle ψ shows a small localized domain (dark blue) of in-plane orientation at the center of the oblate domain, with a strong gradient indicated by the close proximity of the vorticity-aligned domain (dark red). At $t=121$, the single oblate domain at $t=120$ has split into two asymmetric domains; from the director projection

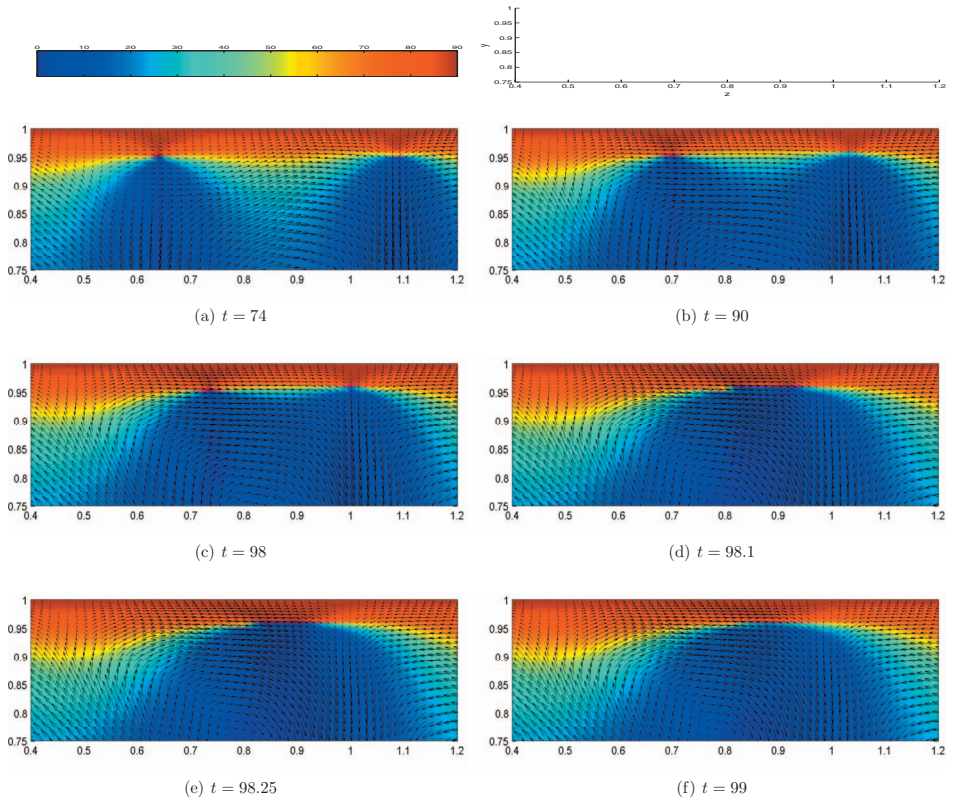

FIG. 11. Diagnostics of defect merger, annihilation of topology, and persistence of oblate domains: seen through the secondary flow field superimposed with color-coded level sets of the director angle ψ with respect to the shear plane. (a) $t=74$, (b) $t=90$, (c) $t=98$, (d) $t=98.1$, (e) $t=98.25$, and (f) $t=99$.

texture, we observe the nucleation of opposite signed, half-integer defects at the center of these two oblate defect domains. From the ψ level sets, we observe that the domain of in-plane orientation has spread with strong gradients now separated and coincident with the oblate domain cores. At $t=123$ and 124, integer defects have now formed, thereby recreating the earlier defect domain structures: two oblate domain cores each carrying a topological defect pair of opposite-signed half-integer and integer winding numbers. The level sets of ψ clearly show a larger domain of in-plane orientation between the separated oblate defect structures, and the sharp blue-red transition of strong gradient of ψ. The defect structures have also migrated closer to the plate, and by $t=126$, they have propagated very near to the top plate.

Closer scrutiny of the secondary flow at $t=126$ shows the flow is sweeping the left defect structure to the right, while the right defect is sitting just above and to the left of a small roll cell, with very little flow either right or left. This flow geometry explains the $t=128$ snapshot where the two defect cores have come closer, and the flow is essentially the same, so these two defects will be drawn yet closer in time, followed by another merger and topological transition.

Integrating further in time, the process continues, at least numerically so, with persistent oblate defects domains with topology attracting one another, oblate domain merger and loss of topology, migration toward the interior, splitting of oblate domains and reformation of topology, propagation toward the plates, *ad infinitum*. This is the defect

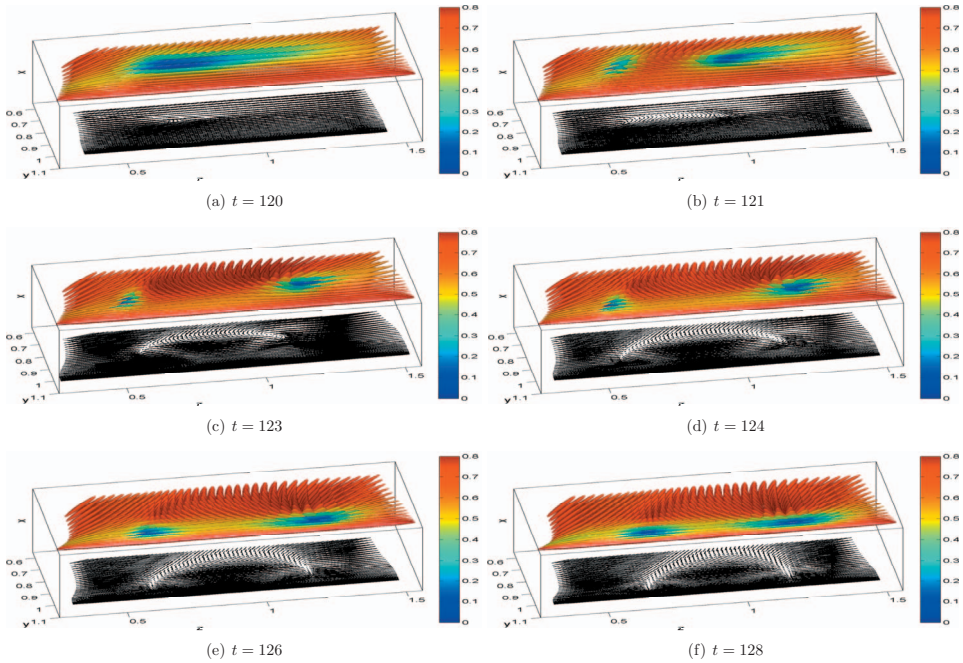

(a) $t = 120$ (b) $t = 121$

(c) $t = 123$ (d) $t = 124$

(e) $t = 126$ (f) $t = 128$

FIG. 12. Diagnostics of oblate defect splitting and reformation of topological degree: seen through the full orientational ellipsoid textures between $t=120$ and $t=128$. (a) $t=120$, (b) $t=121$, (c) $t=123$, (d) $t=124$, (e) $t=126$, and (f) $t=128$.

morphology features of the unsteady attractor that arises from the roll-cell instability. While our simulations and diagnostics share details at specific times with the Klein *et al.* (2007a) and Klein (2007b) studies, there are some differences in the evolution that are almost surely due to the different closure rules employed by the two models. It would be worthwhile to ascertain which model is more faithful to the full kinetic microstructure and Navier–Stokes simulation and to determine which features might be experimentally verified.

IV. CONCLUSION

We have amplified the structure and dynamics of defects that arise in model simulations of the experiments by Larson and Mead on the roll-cell instability, using a combination of local algebraic and nonlocal topological metrics and associated graphics. Klein *et al.* (2007a) and Klein (2007b) presented the first simulations of coupled flow and full tensor orientation dynamics in two space dimensions; we have repeated their simulations with a different closure approximation of the DMG model and a different numerical code. The major new flow-orientation phenomena presented here relate to defect detection, characterization, and evolution with correlations in the secondary flow afforded by full tensor metrics and graphics.

First, we establish that the fundamental defect structure in these flow-coupled systems is an oblate phase arising from a local degree 2 algebraic degeneracy in the leading principal value of the orientation tensor. This degeneracy is trivially detected and imaged through the level sets of the oblate metric $d_1 - d_2$, where d_1 and d_2 are the leading eigenvalues of the second-moment orientation tensor $\mathbf{M}$. Once defects are spawned, our simulations reveal that the oblate domains persist *ad infinitum*, irrespective of topology

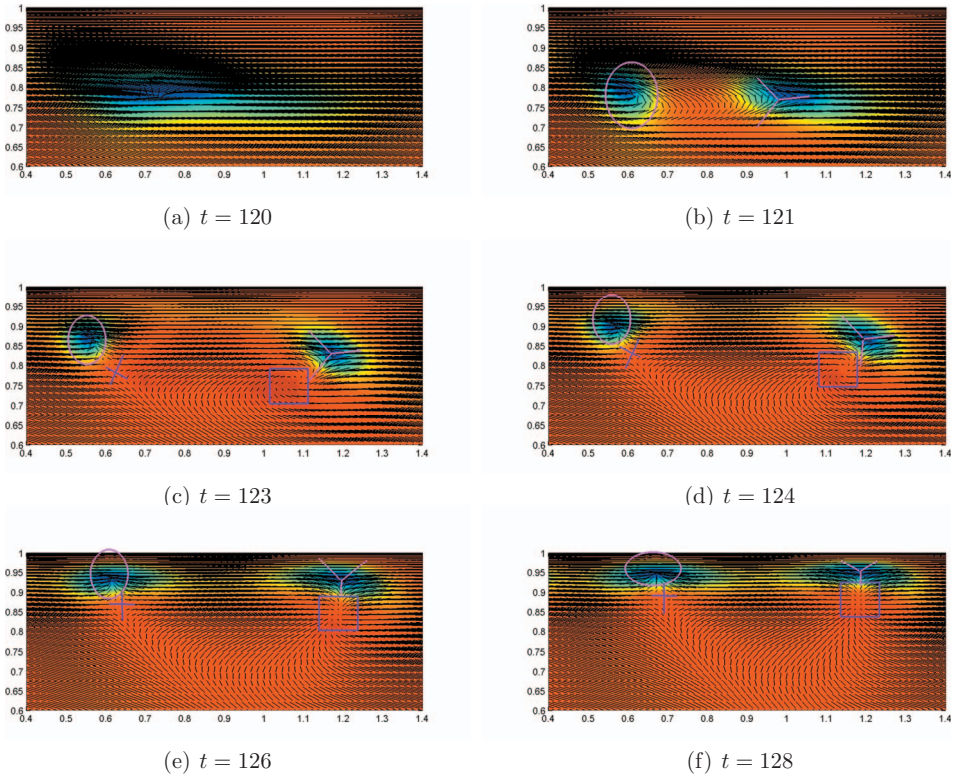

(a) $t = 120$ (b) $t = 121$

(c) $t = 123$ (d) $t = 124$

(e) $t = 126$ (f) $t = 128$

FIG. 13. Diagnostics of oblate defect splitting and reformation of topological degree: seen through the projection of the major director and the color-coded level sets of the oblate defect metric $d_1 - d_2$ between $t=120$ and $t=128$. Topological defects: +1 (square); $-\frac{1}{2}$ (tripod); -1 (cross), and $+\frac{1}{2}$ (circle). (a) $t=120$, (b) $t=121$, (c) $t=123$, (d) $t=124$, (e) $t=126$, and (f) $t=128$.

associated with the projection of the principal axis of **M**. Indeed, oblate defect domains remain clearly identified while the topology surrounding each oblate domain varies among three distinct types during stages of the flow-orientation evolution.

One long-lived topological defect structure consists of an oblate domain with a half-integer defect sitting at the center where $d_1 - d_2 = 0$ and $d_1 > d_3$, and an integer defect of opposite sign translated a small distance from, yet sharing the same oblate domain. Whenever such a defect structure appears, there is a twin structure with opposite-signed topology of both integer and half-integer degrees. The integer defects are always nondegenerate, as seen from the texture of full orientation tensor ellipsoids; the integer defect center corresponds to director escape into the transverse dimension. The half-integer defects are truly degenerate structures associated with the oblate phase core in which the principal axis spreads to a circle.

The second long-lived defect structure has trivial topology, yet the oblate defect domains continue to be identified by level set color coding of the oblate metric $d_1 - d_2$. Traditional diagnostics that focus on topology or on the isotropic phase would therefore fail to identify these persistent defect structures. It is essentially cost free to numerically monitor the isotropic $(d_1 - d_3)$ and oblate $(d_1 - d_2)$ metrics. The simulations therefore smoothly track the remnants of topological structure through oblate metric level sets, which we show are the sources of subsequent transitions back to nontrivial topology as oblate defect domains split. [Oblate defects without topology are not without precedent:

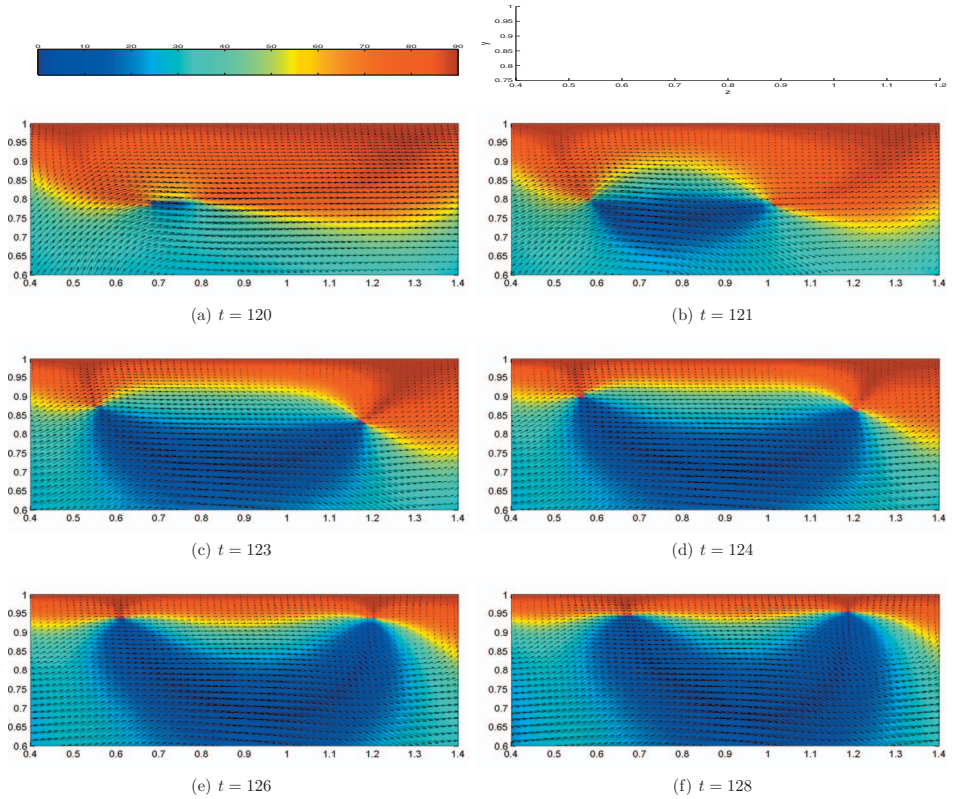

(a) $t = 120$ (b) $t = 121$

(c) $t = 123$ (d) $t = 124$

(e) $t = 126$ (f) $t = 128$

FIG. 14. Diagnostics of oblate defect splitting and reformation of topological degree: seen through the secondary flow field superimposed with color-coded level set values of the out-of-plane director angle ψ. (a) $t = 120$, (b) $t = 121$, (c) $t = 123$, (d) $t = 124$, (e) $t = 126$, and (f) $t = 128$.

in Heidenreich (2008a), we find 1D heterogeneous structures that are stable to 2D perturbations, and which have periodic oblate defect domains with trivial topology.] The third short-lived defect structure consists of an oblate domain with only one half-integer defect sitting over the core, which forms in the transition between the two long-lived structures.

ACKNOWLEDGMENTS

The authors thank the referees for helpful suggestions. This research was supported in part by the Air Force Office of Scientific Research under Contract Nos. F49550-05-1-0025, FA9550-06-1-0063, and FA9550-08-1-0107, the National Science Foundation Grant Nos. DMS-0605029, 0626180, 0548511, 0604891, and 0724273, the Army Research Office under Contract No. 47089-MS-SR, and the NASA URETI BIMat under Award No. NCC-1-02037.

References

Andrienko, D. and M. Allen, "Molecular simulation and theory of a liquid crystalline disclination core," Phys. Rev. E **61**, 504–510 (2000).

Biscari, P. and E. G. Virga, "Local stability of biaxial nematic phases between two cylinders," Int. J. Non-Linear Mech. **32**, 337–351 (1997).

Callan-Jones, A. C., R. A. Pelcovits, V. A. Slavin, S. Zhang, D. H. Laidlaw, and G. B. Loriot, "Simulation and visualization of topological defects in nematic liquid crystals," Phys. Rev. E **74**, 061701 (2006).

Chaubal, C. V. and L. G. Leal, "A closure approximation for liquid-crystalline models based on parametric density estimation," J. Rheol. **42**, 177–202 (1998).

Choate, E. P., M. G. Forest, L. Yao, X. Zheng, and R. Zhou "A simple model for non-topological defects in sheared nematic polymer monodomains," DCDS-B, in press (2009).

Cui, Z., M. G. Forest, Q. Wang, and H. Zhou, "On weak plane Couette and Poiseuille flows of rigid rod and platelet ensembles," SIAM J. Appl. Math. **66**, 1227–1260 (2006).

de Gennes, P.-G., "Phenomenology of short-range-order effects in the isotropic phase of nematic materials," Phys. Lett. **30A**, 454–455 (1969).

de Gennes, P.-G. and J. Prost, *The Physics of Liquid Crystals* (Oxford University Press, New York, 1993).

de Luca, G. and A. D. Rey, "Dynamic interactions between nematic point defects in the extrusion duct of spiders," J. Biol. Phys. **124**, 144904 (2006).

Doi M., "Molecular dynamics and rheological properties of concentrated solutions of rodlike polymers in isotropic and liquid crystalline phases," J. Polym. Sci., Polym. Phys. Ed. **19**, 229–243 (1981).

Doi, M. and S. F. Edwards, *The Theory of Polymer Dynamics* (Oxford University Press, London, 1986).

Feng, J., C. V. Chaubal, and L. G. Leal, "Closure approximations for the Doi theory: Which to use in simulating complex flows of liquid-crystalline polymers?" J. Rheol. **42**, 1095–1119 (1998).

Feng, J. J. and L. G. Leal, "Simulating complex flows of liquid-crystalline polymers using the Doi theory," J. Rheol. **41**, 1317–1335 (1997).

Feng, J. J., J. Tao, and L. G. Leal, "Rolls cells and disclinations in sheared nematic polymers," J. Fluid Mech. **449**, 179–200 (2001).

Forest, M. G. and Q. Wang, "The role of microstructure in taming the Rayleigh capillary instability of cylindrical jets," Physica D **123**, 161–182 (1998).

Forest, M. G. and Q. Wang, "Monodomain response of finite-aspect-ratio macromolecules in shear and related linear flows," Rheol. Acta. **42**, 20–46 (2003).

Forest, M. G., Q. Wang, and H. Zhou, "Nonhomogeneous patterns with core defects in elongational flows of liquid crystal polymers," J. Rheol. **43**, 1573–1582 (1999).

Forest, M. G., Q. Wang, and H. Zhou, "Homogeneous biaxial patterns and director instabilities of liquid crystal polymers in axial and planar elongation," Phys. Fluids **12**, 490–498 (2000a).

Forest, M. G., Q. Wang, and H. Zhou, "Exact banded patterns from a Doi-Marrucci-Greco model of nematic liquid crystal polymers," Phys. Rev. E **61**, 6655–6672 (2000b).

Forest, M. G., Q. Wang, and H. Zhou, "Methods for the exact construction of mesoscale spatial structures in liquid crystal polymers," Physica D **152**, 288–309 (2001a).

Forest, M. G., Q. Wang, and H. Zhou, "On the flow-phase diagram for discotic liquid crystals in uniaxial extension and compression," Liq. Cryst. **28**, 717–720 (2001b).

Forest, M. G., Q. Wang, H. Zhou, and R. Zhou, "Structure scaling properties of confined nematic polymers in-plane Couette cells: The weak flow limit," J. Rheol. **48**, 175–192 (2004c).

Forest, M. G., Q. Wang, and Q. Zhou, "The weak shear kinetic phase diagram for nematic polymers," Rheol. Acta. **43**, 17–37 (2004a).

Forest, M. G., Q. Wang, and R. Zhou, "The flow-phase diagram of Doi–Hess theory for sheared nematic polymers, II: Finite shear rates," Rheol. Acta. **44**, 80–93 (2004b).

Forest, M. G., Q. Wang, and R. Zhou, "Kinetic structure simulations of nematic polymers in-plane Couette cells, II: In-plane structure transitions," Multiscale Model. Simul. **4**, 1280–1304 (2005b).

Forest, M. G., H. Zhou, and Z. Wang, "Anchoring-induced structure transitions of flowing nematic polymers in-plane Couette cells," Discrete Contin. Dyn. Syst., Ser. B **8**, 707–733 (2007a).

Forest, M. G., R. Zhou, and Q. Wang, "Nanorod suspension flows: A 2D Smoluchowski-Navier–Stokes solver," IJNAM **4**, 478–488 (2007b).

Grosso, M., R. Keunings, S. Crescitelli, and P. L. Maffettone, "Prediction of chaotic dynamics in sheared liquid crystalline polymers," Phys. Rev. Lett. **86**, 3184–3187 (2001).

Guermond, J. L. and J. Shen, "On the error estimates of rotational pressure-correction projection methods," Math. Comput. **73**, 1719–1737 (2004).

Han, W. H. and A. D. Rey, "Theory and simulation of optical banded textures of nematic polymers during shear flow," Macromoleclues **28**, 8401–8408 (1995).

Heidenreich, S., M. G. Forrest, S. Hess, S. Klapp, X. Yang, Q. Wang, and R. Zhou, *The XVth International Congress on Rheology*, The Society of Rheology 80th Annual Meeting, Monterey, CA, 3–8 August 2008, edited by A. Co, G. Leal, R. Colby, and A. J. Giacomin, AIP Conf. Proc. No. 1027, Materials Physics and Applications (2008a).

Heidenreich, S., S. Hess, M. G. Forest, X. Yang, and R. Zhou, "Robustness of pulsating jetlike layers in sheared nanorod dispersions," J. Non-Newtonian Fluid Mech. **155**, 130–145 (2008b).

Hess S., "Fokker-Planck-equation approach to flow alignment in liquid crystals," Z. Naturforsch. Teil A **31**, 1034–1037 (1976).

Klein, D. H., Ph. D. thesis, University of California, Santa Barbara (2007b).

Klein D. H., C. J. Garcia-Cervera, H. D. Ceniceros, and L. G. Leal, "Ericksen number and Deborah number cascade predictions of a model for liquid crystalline polymers for simple shear flow," Phys. Fluids **19**, 023101 (2007a).

Klein, D. H., C. J. Garcia-Cervera, H. D. Ceniceros, and L. G. Leal, "Three-dimensional shear driven dynamics of polydomain textures and disclination loops in liquid crystalline polymers," J. Rheol. **52**, 837–863 (2008).

Kleman, M., *Points, Lines and Walls: Liquid Crystals, Magnetic Systems and Various Ordered Media* (Wiley, New York, 1977).

Kleman, M. and J. Friedel, "Lignes de dislocation dans les cholestériques," J. Phys. Colloq. **30**, C4–43 (1969).

Kleman, M. and O. D. Lavrentovich, *Soft Matter Physics* (Springer, New York, 2003).

Kralj S., R. Rosso, and E. G. Virga (private communication).

Kroger, M., "Simple models for complex nonequilibrium fluids," Phys. Rep. **390**, 453–551 (2004).

Kupferman, R., M. N. Kawaguchi, and M. M. Denn, "Emergence of structure in a model of liquid crystalline polymers with elastic coupling," J. Non-Newtonian Fluid Mech. **91**, 255–271 (2000).

Larson, R. G., "Arrested tumbling in shearing flows of liquid crystal polymers," Macromolecules **23**, 3983–3992 (1990).

Larson, R. G., *The Structure and Rheology of Complex Fluids* (Oxford University Press, New York, 1999).

Larson, R. G. and D. W. Mead, "Development of orientation and texture during shearing of liquid-crystalline polymers," Liq. Cryst. **12**, 751–768 (1992).

Larson, R. G. and D. W. Mead, "The Ericksen number and Deborah number cascades in sheared polymeric nematics," Liq. Cryst. **15**, 151–169 (1993).

Larson, R. G. and H. Ottinger, "The effect of molecular elasticity on out-of-plane orientations in shearing flows of liquid crystalline polymers," Macromolecules **24**, 6270–6282 (1991).

Marrucci, G. and F. Greco, "The elastic constants of Maier-Saupe rodlike molecule nematics," Mol. Cryst. Liq. Cryst. **206**, 17–30 (1991).

Marrucci, G. and F. Greco, "Flow behavior of liquid crystalline polymers," Adv. Chem. Phys. **86**, 331–404 (1994).

Meyer, R. B., "On the existence of even indexed disclinations in nematic liquid crystals," Philos. Mag. **27**, 405–424 (1973).

Mottram, N. J. and S. J. Hogan, "Disclination core structure and induced phase change in nematic liquid crystals," Philos. Trans. R. Soc. London, Ser. A **355**, 2045–2064 (1997).

Onogi, S. and T. Asada, in *Rheology, and Rheo-optics of Polymer Liquid crystals in Rheology*, Proceedings of 8th International Congress on Rheology, Vol. 1, edited by G. Astrarita, G. Marruci, and L. Nicholais (Plenum, NY, 1980), pp. 127–147.

Rey, A. D. and M. M. Denn, "Dynamical phenomena in liquid-crystalline materials," Annu. Rev. Fluid Mech. **34**, 233–266 (2002).

Rosso, R. and G. Virga, "Metastable nematic hedgehogs," J. Phys. A **29**, 4247–4264 (1996).

Schopohl, N. and T. Sluckin, "Defect core structure in nematic liquid crystals," Phys. Rev. Lett. **59**, 2582–2584 (1987).

Sgalari, G., L. G. Leal, and J. J. Feng, "The flow behavior of LCPs based on a generalized Doi model with

distortional elasticity," J. Non-Newtonian Fluid Mech. **102**, 361–382 (2002).

Sgalari, G., L. G. Leal, and E. Meiburg, "Texture evolution of sheared LCPs: Numerical predictions of roll-cell instability, director turbulence and striped texture with the molecular model," J. Rheol. **47**, 1417–1444 (2003).

Shen, J., "Efficient spectral-Galerkin method I. Direct solvers for second and fourth-order equations using Legendre polynomials," SIAM J. Sci. Comput. (USA) **15**, 1489–1505 (1994).

Sigillo, I., F. Greco, and G. Marrucci, "Model of a disclination core in nematics," Liq. Cryst. **24**, 419–425 (1998).

Smalyukh, I. I. and O. D. Lavrentovich, in *Defects, Surface Anchoring, and Three-Dimensional Director Fields in the Lamellar Structure of Cholesteric Liquid Crystals as Studied by Fluorescence Confocal Polarizing Microscopy, Topology in Condensed Matter*, edited by M. I. Monastyrsky (Springer, New York, 2006).

Sonnet, A., A. Kilian, and S. Hess, "Alignment tensor versus director: Description of defects in nematic liquid crystals," Phys. Rev. E **52**, 718–722 (1995).

Tan, Z. and G. C. Berry, "Studies on the texture of nematic solutions of rodlike polymers, 3: Rheo-optical and rheological behavior in shear," J. Rheol. **47**, 73–104 (2003).

Tao, J. and J. J. Feng, "Effects of elastic anisotropy on the flow and orientation of sheared nematic liquid crystals," J. Rheol. **47**, 1051–1070 (2003).

Tsuji, T. and A. D. Rey, "Effect of long range order on sheared liquid crystalline materials, Part I: Compatibility between tumbling and behavior and fixed anchoring," J. Non-Newtonian Fluid Mech. **73**, 127–152 (1997).

Tsuji, T. and A. D. Rey, "Orientational mode selection mechanisms for sheared nematic liquid crystalline materials," Phys. Rev. E **57**, 5609–5625 (1998).

Tsuji, T. and A. D. Rey, "Effect of long range order on sheared liquid crystalline materials: Flow regimes, transitions, and rheological diagrams," Phys. Rev. E **62**, 8141–8151 (2000).

Virga, E. G., *Variational Theories for Liquid Crystals* (Chapman and Hall, London, 1994).

Wang Q., "A hydrodynamic theory of nematic liquid crystalline polymers of different configurations," J. Chem. Phys. **116**, 9120–9136 (2002).

Wincure, B. and A. D. Rey, "Heterogeneous curved moving nematic-isotropic fronts," J. Chem. Phys. **124**, 244902 (2006).

Wincure, B. and A. D. Rey, "Nanoscale analysis of defect shedding from liquid crystal interfaces," Nano Lett. **7**, 1474–1479 (2007a).

Wincure, B. and A. D. Rey, "Computational modeling of nematic phase ordering by film and droplet growth over heterogeneous substrates," Liq. Cryst. **34**, 1397–1413 (2007b).

Yang, X., Z. Cui, M. G. Forest, Q. Wang, and J. Shen, "Dimensional robustness & instability of sheared, semidilute, nanorod dispersions," SIAM Multiscale Model. Simul. **7**, 622–654 (2008).

Zhou, R., M. G. Forest, and Q. Wang, "Kinetic structure simulations of nematic polymers in-plane Couette cells, I: The algorithm and benchmarks," SIAM Multiscale Model. Simul. **3**, 853–870 (2005a).